

UNIVERSIDAD DE LOS ANDES



MASTER THESIS

---

# The effect of gas bulk rotation on the morphology of the Lyman $\alpha$ line

---

*Author:*

Juan Nicolas Garavito Camargo

*Supervisor:*

Dr. Jaime E. Forero Romero

*A thesis submitted in fulfilment of the requirements  
for the degree of Master in Physics*

*in the*

Astronomy group  
Physics Department

April 2015

*“It would obviously be rewarding if our current theoretical ideas are confirmed by future observations, but it might be even more exciting if this ideas are modified.”*

Abraham Loeb

## *Acknowledgements*

I feel very gratefull with the departament of physics of the Andes Univserity for providing a confortable and motivating atmosphere. In which learning and devloping new skills is very .. I also want to thank the astronomy group leading by Dr. Jaime Forero in which...

# Contents

<b>Acknowledgements</b>	<b>ii</b>
<b>Contents</b>	<b>iii</b>
<b>List of Figures</b>	<b>v</b>
<b>List of Tables</b>	<b>vii</b>
<b>1 Introduction</b>	<b>1</b>
1.1 <i>Motivation</i>	1
1.2 <i>Historical Remarks</i>	2
1.3 <i>The Lyman <math>\alpha</math> line in astronomy</i>	3
1.4 Units, Quantities & Definitions	3
1.4.1 Optical depth and Column Density	4
1.4.2 Ly $\alpha$ line profile units	4
1.4.3 Average number of scatterings $N_{scatt}$	5
1.4.4 Resonant scattering	5
1.4.5 Escape fraction	7
1.5 <i>Attenuation of the Ly<math>\alpha</math> emission line</i>	7
1.6 <i>Analytical Models</i>	9
1.6.1 Infinite Slab with Ly $\alpha$ source at the center:	10
1.6.2 Spherical solution	11
1.6.3 Spherical rotating sphere	12
1.7 <i>Simulated models &amp; techniques</i>	12
1.7.1 Monte-Carlo approach:	12
1.7.2 Numerical Models of Ly $\alpha$ profiles:	13
1.8 <i>This Thesis</i>	14
1.8.1 The importance of modelling the effect of gas bulk rotation	14
1.8.2 Summary of the thesis	14
1.8.3 Future work	15
<b>2 The effect of gas bulk rotation on the morphology of the Ly<math>\alpha</math> line</b>	<b>17</b>
2.1 Introduction	18
2.2 Models of bulk gas rotation	19
2.2.1 Detailed Implementation of Rotation	20
2.2.2 Brief Description of the Radiative Transfer Codes	21

2.2.3	Grid of Simulated Galaxies . . . . .	23
2.3	Results . . . . .	25
2.3.1	Line Morphology . . . . .	25
2.3.2	Integrated Line Intensity . . . . .	26
2.3.3	Full Width at Half Maximum . . . . .	27
2.3.4	Line Maxima . . . . .	28
2.3.5	Dusty Clouds: Escape Fraction . . . . .	29
2.3.6	Average Number of Scatterings . . . . .	30
2.4	Discussion . . . . .	31
2.4.1	Towards an analytical description . . . . .	31
2.4.2	Impact on the interpretation of simulated and observational data . . . . .	32
2.5	Conclusions . . . . .	33
.1	Analytic Expression for the Ly $\alpha$ Spectrum emerging from Rotating Cloud . . . . .	35

<b>A</b>	<b>Analytic Expression for the Ly<math>\alpha</math> Spectrum emerging from Rotating Cloud</b>	<b>38</b>
----------	--	-----------

<b>Bibliography</b>	<b>41</b>
---------------------	-----------

# List of Figures

1.1	Scattering scheme of a Ly $\alpha$ photon in a HI medium (The star is a Ly $\alpha$ source and the solid line represents the path that the Ly $\alpha$ photon follow before scaping the cloud).	6
1.2	Scheme of the frequency shift. Left: Rest frame, Because of the velocity $u$ of the atom absorb a blue-shifted Ly $\alpha$ photon, and emmit a red-shifted Ly $\alpha$ photon. Right HI atom rest frame when all photons have the Ly $\alpha$ frequency. (Image credit: Interpereting Lyman $\alpha$ radiation from young, dusty galaxies. By: Peter Laursen, 2010.).	6
1.3	The IGM effect on the Ly $\alpha$ line	8
1.4	Asymmetry and multi peaked Ly $\alpha$ line profiles. (Image credit: The kinematics of multiple-peaked Ly $\alpha$ emission in star-forming galaxies at $z \sim 2 - 3$ . Kulas, K. et al 2011)	8
1.5	(left) Analytic profile for a dustless infinite slab with central Ly $\alpha$ souces. (Middle) Maximum peaks position. (Right) Average number of scatterings $N_{scatt}$ in function of the optical depth $\tau$ . (Image credit: CLARA's view on the escape fraction of Ly $\alpha$ photons in high redshift galaxies. J.E Forero-Romero, et al 2011)	11
1.6	Analytic profile for a dustless sphere with central Ly $\alpha$ sources. (Image credit: CLARA's view on the escape fraction of Ly $\alpha$ photons in high redshift galaxies. J.E Forero-Romero, et al 2011)	11
2.1	Geometry of the gas distribution. The angular velocity vector is parallel to the unit vector $\hat{k}$ . In order to describe the departures from spherical symmetry we use the polar angle $\theta$ formed by the direction of the outgoing photons with respect to the $z$ -axis. We define the variable $\mu \equiv \cos \theta$ to report to present our results. Computing the spectra for photons in a narrow range of $\mu$ is equivalent to having a line-of-sight oriented in that direction.	20
2.2	2D histogram showing the number of photons that escape with frequency $x$ forming an angle $\theta$ (parametrized as $ \cos \theta $ ) with the rotation axis. The rotational velocity (0, 100, 200, 300 km s $^{-1}$ ) increases from left to right and the optical depth ( $10^5$ , $10^6$ , $10^7$ ) from top to bottom. The Ly $\alpha$ photons are initialized at the center of the sphere. Two main results can be read from this figure. First, the line morphology depends on the viewing angle. Second, the line can become single peaked for high rotational velocities.	21
2.3	Same as Fig. 2.2 for Ly $\alpha$ photons initialized homogeneously throughout the sphere.	22

2.4	Shape of the Ly $\alpha$ line for different maximum rotational velocities for a LoS perpendicular to the rotation axis ( $ \mu  \sim 0$ ). The continuous (dashed) line represents the central (homogeneous) source distributions. The continuous thin line represents the intrinsic homogeneous spectrum. The panels follow the same distribution as in Figs 2.2 and 2.3. . . . .	23
2.5	Shape of the Ly $\alpha$ line for different maximum rotational velocities for a LoS perpendicular to the rotation axis ( $ \mu  \sim 1$ ). The continuous (dashed) line represents the central (homogeneous) source distributions. The continuous thin line represent the intrinsic homogeneous spectrum. The panels follow the same distribution as in Figs 2.2 and 2.3. . . . .	24
2.6	Integrated flux distribution as a function of the viewing angle as parametrized by $\mu$ . Continuous (dashed) correspond to central (homogeneous) source distribution. The models correspond to an optical depth of $\tau_H = 10^5$ and rotational velocities of $100 \text{ km s}^{-1}$ , $200 \text{ km s}^{-1}$ and $300 \text{ km s}^{-1}$ . The distributions are flat in the range of models probed in this paper, meaning that the integrated flux for all viewing angles is the same. . . . .	26
2.7	FWHM for the non-dusty models as a function of the viewing angle parametrized by $ \cos \theta $ . Continuous (dashed) lines correspond to central (homogeneous) source distributions. The general trend is of an decreasing line width as the line of sight becomes parallel to the rotation axis. . . .	27
2.8	FWHM for the non-dusty models as a function of rotational velocity $V_{\text{max}}$ for observers located perpendicular to the rotation axis. The left panel shows the results in velocity units while the right panel normalizes the data by the FWHM in the static case. Continuous (dashed) lines correspond to central (homogeneous) source distributions. The straight lines represent the fit to the data using the expression in Eq. (2.5). . . . .	27
2.9	Position of the line maxima as a function of maximum rotational velocity $V_{\text{max}}$ . Continuous (dashed) lines correspond to central (homogeneous) source distributions. A value of $x_{\text{max}} = 0$ indicates that line becomes single peaked. . . . .	28
2.10	2D histogram of the logarithm of the average number of scatterings as function of $\mu$ (left) and the maximum rotational velocity $V_{\text{max}}$ (right). The left panel shows the behaviour for $\tau = 10^5$ and $V_{\text{max}} = 300 \text{ km s}^{-1}$ as a function of $ \cos \theta $ , the color indicates the number of photons per bin. In the right panel the continuous (dashed) lines represent the results for the central (homogeneous) model. The independence of $N_{\text{scatt}}$ with $\mu$ and $V_{\text{max}}$ is present in all models. . . . .	30
2.11	Comparison of the Monte Carlo results against the analytic solution. The left panel explores the results of different velocities. The right panel presents the results for two different observers: paralel and perpendicular to the rotational axis, $\mu = 1$ and $\mu = 0$ respectively. . . . .	32

# List of Tables

2.1	Summary of Physical Parameters of our Monte Carlo Simulations. . . . .	24
2.2	Escape fraction values for all dusty models. . . . .	29



*To my parents: Vilma & Edgar*

# Chapter 1

## Introduction

### 1.1 *Motivation*

It is astonishing how much we can learn from observing and contemplating the Universe. All this knowledge of the Universe led to a better comprehension of the dynamics of the Universe itself and how its components galaxies, interstellar/intergalactic medium and stars has evolved in time. This theories doesn't have just an academic impact, society have faced different changes of paradigm due to this scientific achievements. And hopefully this knowledge of nature can help us in the path to a modern sustainable society with the conscious of our place and role in the Universe.

Astronomy is unique in the sense that there is only one Universe to observe. Due to the expanding nature of the Universe and that the speed of light is finite, observations of the farther regions of the Universe are also from the youngest stages of the Universe. This allows to observe the evolution of the Universe during redshift.

There are two techniques to measure the radiation coming from the Universe; photometry and spectroscopy. Photometric observations measures the flux astronomical objects in different filters. This allows to derive quantities such as the luminosity and the temperature. While spectroscopic observations would let study in deep detail the spectra of astronomical objects, in particular the spectra of galaxies reveals properties such as: the population of stars in the galaxy, the redshift, the elements that constitute this objects, the characteristics of the interstellar medium and many more.

In particular the Lyman $\alpha$  emission line is a usefull tool to detect star forming galaxies at high redshift, specially at  $z > 2$  which is when the line is shifted to the optical frame. But as discussed in X the morphology of the line is substantially affected by the gas kinematics & distribution, the interstellar gas (IGM) and by the dust.

Understanding the morphology of the Ly $\alpha$  line is a crucial endeavour to understand deeply the properties of galaxies at high redshift. To this aim computer simulations are extremely useful, models of these properties can be simulated to create synthetic profiles that can be compared with the observations.

This is an important era to study these high redshift galaxies. Computer simulation techniques have been improved and more powerful facilities are now available. Also a new generation of telescopes are being constructed, these telescopes would have the power to observe more deeply in the sky, and new high redshift galaxies are going to be discovered. This would improve our understanding of the high redshift Universe.

## 1.2 *Historical Remarks*

The emission of the Ly $\alpha$  line in galaxies was first predicted by [1] in 1967, in their work they suggest that the Ly $\alpha$  luminosity could amount to the luminosity of the galaxies at high redshift, and that it could be detected by the telescopes.

By the same epoch the radiative transfer theory in Ly $\alpha$  systems started to be studied by [2–5], it can be seen as a diffusion process if it is carried out in an optically thick medium. It means that Ly $\alpha$  photons propagating in a medium are diffusing in space and in wavelength from the line center. Because of the complexity of these systems an analytical solution can only be carried out in simplified systems.

Almost three decades later [6] detected the first Ly $\alpha$  emitter galaxy (LAE), since then hundreds of galaxies have been observed at redshifts  $z > 2$  (citations). There is a confirmed LAE at  $z = 8.6$  by [7] and candidates up to  $z \sim 12$  by [8]. The Ly $\alpha$  line has the potential to be a tool to confirm galaxies at the highest redshifts.

Despite all these observational efforts to fully understand the radiative transfer (RT) of the Ly $\alpha$  line numerical simulations started to be performed. [9–12] in order to understand more realistic situations.

More recently various teams [13, 14] have observed nearby galaxies with the Hubble Space Telescope. With the aim to have a better resolution spectra and images of the H I distribution and kinematics. This new data now can be compared with the numerical models developed.

### 1.3 The Lyman $\alpha$ line in astronomy

The Lyman  $\alpha$  (Here after  $\text{Ly}\alpha$ ) emission line is a consequence of the transition from the first excited level to the ground level of the electrons in the Hydrogen atom. When the electron undergoes in such transition a photon is emitted with an energy of  $13.6\text{eV}$  which corresponds to a rest wavelength of  $1215.67\text{\AA}$ .

This transition is very common in the Universe due to the high abundance of hydrogen. Two main mechanisms end up in  $\text{Ly}\alpha$  radiations: Recombination processes and collisional events of Hydrogen atoms. UV stellar radiation from star regions (Recombination), Gravitational cooling (Collisional) and UV background radiation (Recombination) the interested reader could read [15] and references within for more details.

The detection of the  $\text{Ly}\alpha$  line has been broadly studied and has multiple applications in extragalactic astronomy:

- **Detection of high  $z$  galaxies:** One of the most used methods to detect high redshift galaxies is finding the  $\text{Ly}\alpha$  emission line using narrow band imaging or spectroscopy. With this methods hundreds of galaxies has been detected. This allows to study the properties of the high redshift Universe such as the large scale structure.
- **Galaxy formation and evolution:** Observed LAEs at different reshifts has allowed to derive the Lumimosity Functions (LFs) of LAEs, for this aim a good knowledge of the escape fracition of photons is requiered  $f_{esc}$  see §1.4.5 for details on the escape fraction of  $\text{Ly}\alpha$  photons. As consequence the observed LAEs LFs enhance a better understanding of the galaxy formation processes.
- **Reionization:** The Epoch of Reionization (EoR) is an important period of the Universe, in which the neutral cold HI gas reionize to become a hot gas. There is evidence from CMB measurements that the EoR must start at  $z \gg 11$  and should end up at  $z \sim 5$ . During this epoch the intergalactic medium (IGM) became opaque to the  $\text{Ly}\alpha$  radiation outcomming from the galaxies. LAEs has also shown to be very usefull in constrainig the time at which the EoR ends. For a complete recent review please see [16] and references within.

### 1.4 Units, Quantities & Definitions

Through this work We will use some units and quantities very popular in this area. For clarity here we briefly define and review this quantities and units.

### 1.4.1 Optical depth and Column Density

The optical depth  $\tau$  is a measure of the "transparency" of the medium in which the photons are propagating,  $\tau$  is defined as:

$$d\tau = \alpha dr \quad (1.1)$$

Where  $\alpha$  is the absorption coefficient defined as:

$$\frac{dI}{dr} = -\alpha I \quad (1.2)$$

From this definitions we can now define the "thickness" of the medium. If  $\tau > 1$  we said that the medium is optically thick and this means that a photon with frequency  $\nu$  cannot go through the medium without been absorbed. If  $\tau < 1$  the medium is optically thin and the photon could be pass through the medium with out been absorbed.

The optical depth is a measure of the distance of the source of photons to the surface of the medium. It is also very common to express the amount of gas between the Ly $\alpha$  source and the surface in terms of the Hydrogen column density  $N_{HI}$  which is related with the optical depth by  $N_{HI} = \tau/\sigma$  where  $\sigma$  is the Hydrogen atom cross section.

### 1.4.2 Ly $\alpha$ line profile units

The frequency  $\nu_\alpha$  of a Ly $\alpha$  photon in rest frame is  $2.46 \times 10^{15} Hz$ , there are two new variables  $x, V$  in which the frequency of the Ly $\alpha$  alpha photons may be presented in the literature.

The first is a dimensionless variable  $x$  defined as:

$$x \equiv \frac{(\nu - \nu_\alpha)}{\Delta\nu_D} \quad (1.3)$$

Where  $\nu$  is the frequency in the observer frame,  $\nu_D$  is the broadening of the line due to the thermal velocity of the Hydrogen atoms  $v_{th}$ . This velocity can be derived assuming that the Hydrogen gas is in thermal equilibrium and follows a Maxwellian distribution. In thermal equilibrium we get:

$$\frac{m_H v_{th}^2}{2} = K_B T \quad (1.4)$$

Where  $m_H$  is the Hydrogen atom mass,  $K_B$  the Boltzmann constant and  $T$  the temperature in Kelvins, the expression for  $v_{th}$  is then:

$$v_{th} = \sqrt{\frac{2K_B T}{m_H}} = 128.5 T^{1/2} \frac{m}{s} \quad (1.5)$$

The Doppler shift due to  $v_{th}$  would be:

$$\nu' = \left(1 - \frac{\vec{v}_{th} \cdot \vec{n}}{c}\right) \nu_\alpha \quad (1.6)$$

Which can be expressed in terms of  $\Delta\nu_D$  as:

$$\nu_\alpha - \nu' = \Delta\nu_D = \frac{\vec{v}_{th} \cdot \vec{n}}{c} \quad (1.7)$$

It is also common to express the line profile in terms of the velocity  $V$  making use of Eq.1.3:

$$V = x v_{th} = \frac{\nu - \nu_{\alpha}}{c} \quad (1.8)$$

### 1.4.3 Average number of scatterings $N_{scatt}$

The path of a Ly $\alpha$  photon inside an **optically thick** HI medium is resonant this is explained in more detail in §1.4.4. It basically means that the Ly $\alpha$  photon after being emitted by the source is absorbed by an H atom and re-emitted in a time scale of  $\sim 10^{-9}$  s. For this reason this process is commonly referred as a scattering process. The total number of scatterings is denoted as  $N_{scatt}$  and it is proportional to  $\tau^2$ .

### 1.4.4 Resonant scattering

Hydrogen is the most abundant element in the Universe furthermore the Ly $\alpha$  line is a very common line. However the transmission of this Ly $\alpha$  photons through the Hydrogen clouds is not trivial. There are two main aspects that heavily influence the morphology of the line.

Imagine that there is one Hydrogen atom which emits a Ly $\alpha$  photon in the middle of a cloud of HI. The Ly $\alpha$  photon will be absorbed and re-emitted from the Hydrogen atoms. This process will end up in a random walk in the space, and the photon can escape the

cloud at any point in of the surface, see Fig.??.

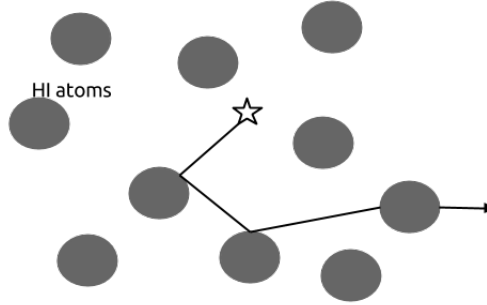


FIGURE 1.1: Scattering scheme of a  $\text{Ly}\alpha$  photon in a HI medium (The star represent a  $\text{Ly}\alpha$  source and the solid line represents the path that the  $\text{Ly}\alpha$  photon follow before scaping the cloud).

In the previous situation all the Hydrogen atoms were in rest, if the atoms present proper motions there would be a doppler shift Fig.?.?. If an atom have a velocity  $v$  an emit a  $\text{Ly}\alpha$  photon in the direction opposite to the movement the  $\text{Ly}\alpha$  photon would be redshifted. But if it is emitted in the same direction of movement the  $\text{Ly}\alpha$  photon would be blueshifted.

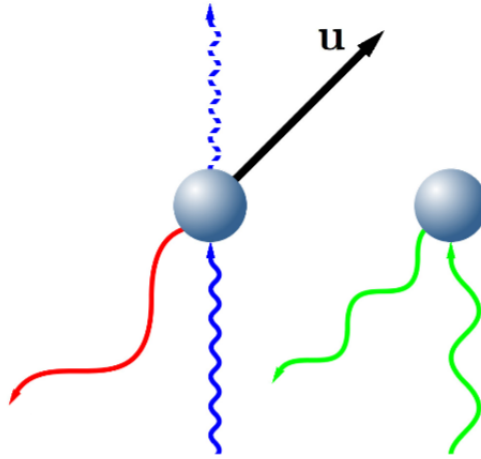


FIGURE 1.2: Scheme of the frequency shift. Left: Rest frame, Because of the velocity  $u$  of the atom absorb a blue-shifted  $\text{Ly}\alpha$  photon, and emmit a red-shifted  $\text{Ly}\alpha$  photon. Right HI atom rest frame when all photons have the  $\text{Ly}\alpha$  frequency. (Image credit: Interpreting Lyman  $\alpha$  radiation from young, dusty galaxies. By: Peter Laursen, 2010.).

This two effects made radiative transfer inside optically thick medium as a random walk in space and frequency. This is why Monte-Carlo methods can be applied to this diffusion process.

### 1.4.5 Escape fraction

Dust grains are mainly considered as metals in the ISM, these metals are formed in stars. At high redshifts where galaxies and stars are young the most probable escenario in that supernovae enrich the ISM with dust [17], in this way the observed dust [18] at high redshift is explained.

The effect of dust in the Ly $\alpha$  transfer inside the ISM is that dust grains can absorb (destroy) or scatter Ly $\alpha$  photons. The probability of this events is given by the 'albedo'  $A$  defined as:

$$A = \frac{\sigma_{scatt}}{\sigma_{dust}} \quad (1.9)$$

Where  $\sigma_{scatt}$  is the total cross section for scattering and  $\sigma_{dust}$  for absorption.  $\sigma_{dust}$  can be derived from dust properties see [10].

There are two approaches to the modelling of dust in the Ly $\alpha$  RT process. As a first approximation the dust distribution is taken as an homogeneous distribution in the HI region and the Ly $\alpha$  photons can be absorbed by the dust or scattered. A more sophisticated situation is that the medium follows a clumpy distribution of dust in which Ly $\alpha$  photons are more likely to scatter with the clumps rather than absorbed [19]. To quantify the effect of the dust the ratio of Ly $\alpha$  photons observed (Ly $\alpha$  alpha photons who manage to scape from the medium) over the Ly $\alpha$  photons emmited define a cuantity call the **escape fraction**  $f_{esc}$ .

It is worth pointing out that the analytical description of the Ly $\alpha$  RT doesn't take into account the precense of dust. That is also a motivation to include dust in the numerical simulations. As is explained in more detail in §1.6.

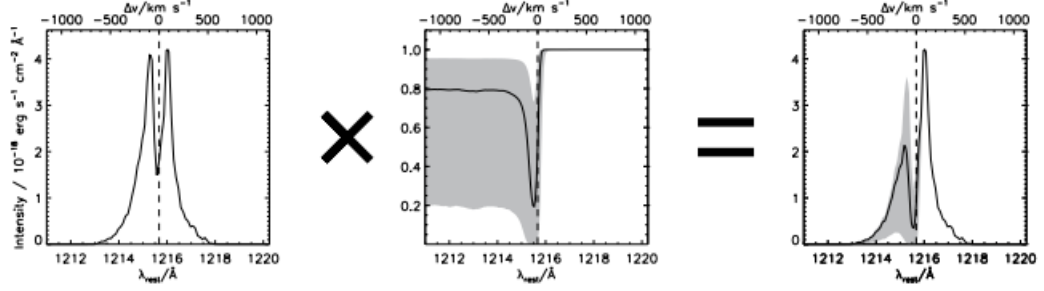
## 1.5 Attenuation of the Ly $\alpha$ emission line

Despite the fact that the Ly $\alpha$  line is the strongest emission line in the UV, there were 25 years since the prediction of the Ly $\alpha$  line to the first observation by [6]. This long absence of the Ly $\alpha$  line is what makes this and excited and challenging field.

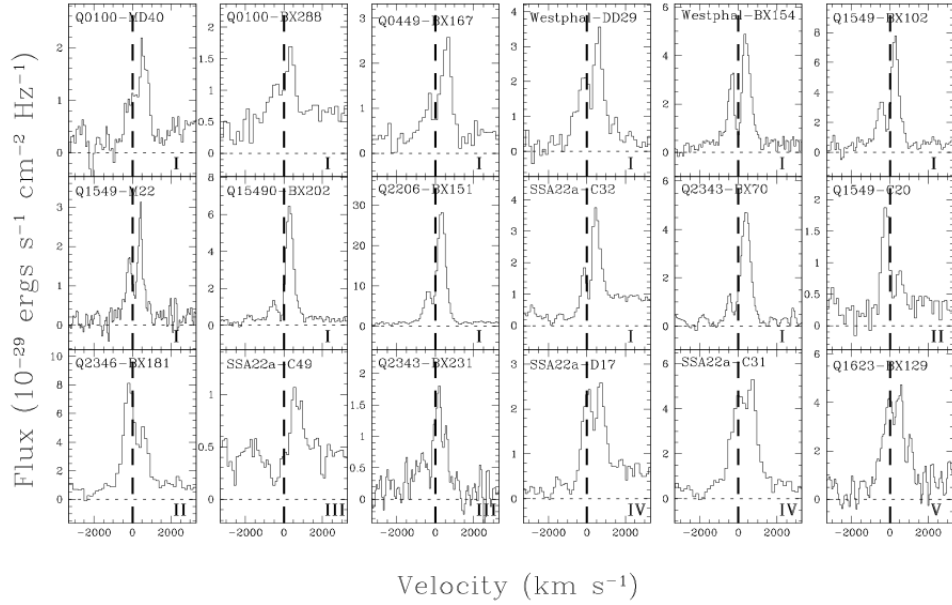
Figure?? shows the outcomming spectra from a galaxy at  $z \sim 3.5$ , the line is double paked as expected from the radiative transfer process in the galaxy. After the encounter with the inter-galactic medium (IGM) de blue peak is diminished. Dut to the expansion of the Universe the blue peak is shifted to the Ly $\alpha$  frequency and the HI in the IGM



[H]

FIGURE 1.3: The IGM effect on the Ly $\alpha$  line

[H]

FIGURE 1.4: Asymmetry and multi-peaked Ly $\alpha$  line profiles. (Image credit: The kinematics of multiple-peaked Ly $\alpha$  emission in star-forming galaxies at  $z \sim 2 - 3$ . Kulas, K. et al 2011)

would absorb part of this radiation. As a result the observed spectra (right figure) is asymmetric.

The gas kinematics in the galaxy also plays a mayor role in shaping the morphology of the line, due to the resonant nature of the line. Figure?? show the Ly $\alpha$  line profile for different galaxies at  $z \sim 2 - 3$ , due to the different kinematics of those galaxies all the spectra reveals asymmmtric profiles and some of them are multi-peaked.

The presence of dust in galaxies also play an important role, dust as explained in §1.4.5 could either absorb or scatter Ly $\alpha$  photons. As a consequence dust mainly diminish

the intensity of the Ly $\alpha$  line of LAEs.

Alongside these processes when observing the abundance of LAEs across the history of the Universe the population of LAEs increases with the redshift. But at redshifts  $z > 6$  the abundance of LAEs decrease [20]. Apparently reionization is governing at that redshift and the IGM medium becomes opaque to Ly $\alpha$  radiation.

All this effects makes the Ly $\alpha$  line a sensitive line and challenging to observe at  $z > 6$  see [21], but with valuable information of the ISM/IGM distribution and kinematics. All this makes de Ly $\alpha$  line a very usefull line to explore the extragalactic Universe as discussed in §1.3.

## 1.6 Analytical Models

Understanding the Ly $\alpha$  line profile requieres a theory knowledge about the physics processes involving the radiatie transfer. Symplified situations have been studied in order to obtain an analytical profile. This models provide the theory that would let developpe the modern codes enable to This models are the foundations. In this section the most relevant analytical models are explained in the chronological in which they have been developed.

The radiave transfer of Ly $\alpha$  photons has been studied by several authors see [22] for a complete treatment, the Intensity of Ly $\alpha$  photons can be studied via:

$$n \cdot \nabla I(\nu, n) = -\alpha_\nu I(\nu, n) + j(\nu, n) + \int d\Omega' \int dn' I(\nu', n') R(\nu', \nu, n', n) \quad (1.10)$$

Where  $\nu$  is the frequency of the Ly $\alpha$  photons.  $n$  is the direction of the Ly $\alpha$  photon.  $I(\nu, n)$  is the intensity of the radiation.  $\Omega$  is the solid angle.  $R(\nu', \nu, n', n)$  is the redistribution function, basically this function which measures the probability that a Ly $\alpha$  photon with frequency  $\nu'$  and direction  $n'$  after scatters have a frequency  $\nu$  and direction  $n$ .

The mean density  $J_\nu$  is defined as:

$$J_\nu = \frac{1}{4\pi} \int I_\nu d\Omega \quad (1.11)$$

Using Eq.1.11 and following the above steps:

- In an optically thick medium the dependece on the direcion  $n$  can be neglected.

- Using a Taylor expansion in  $(I(\nu', n'))$  in the second term of the right in Eq.1.10
- Replacing the absorption coefficient in terms of the optical depth.
- $j(\nu, n) = 0$  and  $\sigma_{dust} = 0$

Eq.1.10 can be expressed as:

$$\frac{dJ(\nu)}{d\tau} = \frac{(\Delta\nu_D)^2}{2} \frac{\partial}{\partial\nu} \phi(\nu) \frac{\partial J(\nu)}{\partial\nu} \quad (1.12)$$

Where  $\phi(\nu)$  is a Voigt profile (Combolution of a Gaussian profile and Lorentzian profile), this Voigt profiles respond to the resonant nature of the line. Eq.1.12 is a diffusion equation in space and frequency for the Ly $\alpha$  photons in HI clouds. Different authors have solved Eq.1.10 in simplified situations that we are going to discuss above.

### 1.6.1 Infinite Slab with Ly $\alpha$ source at the center:

The first analytical solution to the RT Eq.1.12 was an effort in which different authors made a contributions [2–4, 23] and ended with the analytical expresion derived by [?] based on the previous works.

$$J(\tau_0, x) = \frac{\sqrt{6}}{24} \frac{x^2}{\sqrt{\pi} a \tau \cosh[\sqrt{\pi^3/54}(x^3 - x_{in}^3)/a\tau]} \quad (1.13)$$

Where  $a$  is the Voigt parameter defined as  $a = A/4\pi\Delta\nu_D$ . [4] also show that the maximum intensity of the line is at:

$$x_m = \pm 1.066(a\tau)^{1/3} \quad (1.14)$$

And the average number of scatterings is:

$$N_{scatt} = 1.612\tau \quad (1.15)$$

In Fig.?? the analytical profile of the slab solution is shown, the solid line is the simulated profile reproduced with [12] the code used in this work.

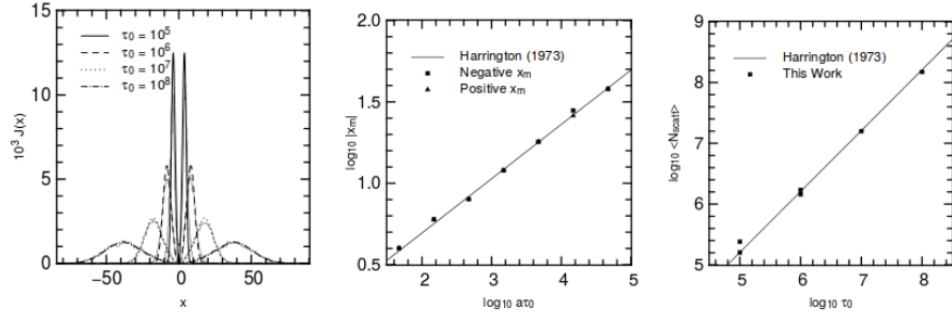


FIGURE 1.5: (left) Analytic profile for a dustless infinite slab with central Ly $\alpha$  sources. (Middle) Maximum peaks position. (Right) Average number of scatterings  $N_{scatt}$  in function of the optical depth  $\tau$ . (Image credit: CLARA's view on the escape fraction of Ly $\alpha$  photons in high redshift galaxies. J.E Forero-Romero, et al 2011)

### 1.6.2 Spherical solution

For a spherical gas dustless distribution with central Ly $\alpha$  sources [24] has shown that the emergent spectrum is described by the following expression:

$$J(\tau_0, x) = \frac{\sqrt{\pi}}{4\sqrt{6}} \frac{x^2}{a\tau(1 + \cosh[\sqrt{2\pi^3/27}x^3/a\tau])} \quad (1.16)$$

The analytical spectrum of the spherical solution is shown in Fig.?? for different optical depths.

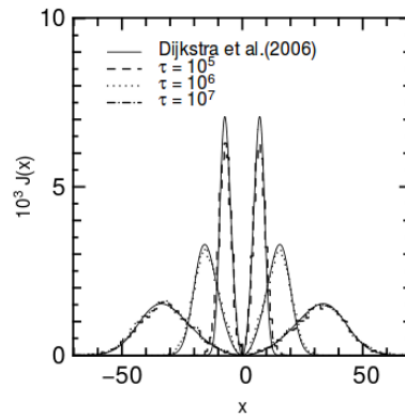


FIGURE 1.6: Analytic profile for a dustless sphere with central Ly $\alpha$  sources. (Image credit: CLARA's view on the escape fraction of Ly $\alpha$  photons in high redshift galaxies. J.E Forero-Romero, et al 2011)

### 1.6.3 Spherical rotating sphere

In this work Mark Dijkstra has shown also that an approximate analytical profile can be derived for a **rotating spherical distribution** Eq.1.17 with central sources and dustless. This would be the first time that an analytic al profile is derived for a non-static medium.

$$J(x, b, \phi, i) = \frac{\sqrt{\pi}}{\sqrt{24}a\tau_0} \left( \frac{(x - x_b)^2}{1 + \cosh \left[ \sqrt{\frac{2\pi^3}{27}} \frac{|(x - x_b)^3|}{a\tau_0} \right]} \right) \quad (1.17)$$

$$J(x, i) = 2\pi \int_0^R db b \int_0^{2\pi} d\phi S(b, \phi) J(x, b, \phi, i) \approx 2\pi \int_0^R db b \int_0^{2\pi} d\phi J(x, b, \phi, i)$$

## 1.7 Simulated models & techniques

In the Universe most of the galaxies have complicated geometries (Spirals, irregular) and kinematics that can not be resolved analitically. There are two approaches to uderstant this complicated properties of galaxies, based on Monte-Carlo simulations. The first approach is by implementing the properties of galaxies in the codes, such as: The geometry of the gas, the kinematics of the gas and the dust. In this approach every property is isolated simulated in order to compute the Ly $\alpha$  profiles, escape fractions, average number of scatterings, position of the maximum peaks among others.

Realistic galaxy properties in the sense of gas geometry and kinematics using hydrodynamics simulations. In this approach the galaxy can be simulated isolated see [25] or galaxies in the cosmic web can also be studied see[26]. The temperature, density and gas velocity fields are obtained from the hydrodinamic simulations and then the Monte-Carlo code is implemented in order to compute the profile properties.

### 1.7.1 Monte-Carlo approach:

Monte-Carlo (MC) simulations are broadly used in a varierty of areas such as science, economy, traffic simulatios among many more. MC methods are mostly based in the generation of random numbers that are the core of random walks. This is why MC is used to study the Ly $\alpha$  profile. Here we breaffly describe how this method work. The main thing is that every every Ly $\alpha$  photon is simulated separately in the following scheme, for a detailed description please see chapters 6 – 8 in [15] .

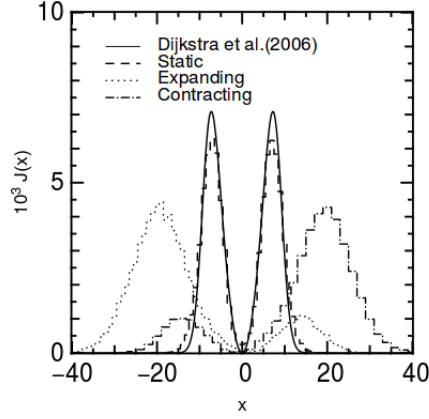
- The temperature (T) is very common to take  $T = 10^4 K$ , gas distribution ( $\tau$ ) and kinematics ( $V$ ) is implemented.
- Initialize your Ly $\alpha$  photon initial position and frequency  $x_{in}$
- Generate a random displacement ( $\tau_0$ ) of the photon in a random direction  $\vec{n}$ .
- Derive the HI atom velocity components from the initial field, and generate random components for the thermal movements.
- Set the new direction of the Ly $\alpha$  photon after scattering.
- If the Ly $\alpha$  photon encounter a dust particle the albedo probability would define if the atom is absorbed or scattered. In also common to take  $A = 1/2$
- Repeat from step 2 untill the photon reaches the HI surface at  $\tau$ .

With this method the final frequency  $x_{out}$ , the average number of scatterin gs  $N_{scatt}$  can be computed for every step in the random walk.

### 1.7.2 Numerical Models of Ly $\alpha$ profiles:

Using the MC method explained above different RT codes [9–12] have been developed in order to understand the effect of the gas kinematics in the Lyman  $\alpha$  line, expanding/-contracting shell/spherical geometries has been broadly studied [11, 24, 27]. Realistic ISM/IGM medium has also been studied, the effect of a clumpy medium is discussed in [28]. Anysotropic Ly $\alpha$  emission has been studied by [29]. And realistic exapanding mediums in cavities has been recently studied by [30] Hydrodynamic simulations have studied the outcomming spectra of LAEs in large scale simulations [31]. Recently Monte Carlo codes have been used in hydrodynamic simulations to study in detail individual galaxies and galaxies in the cosmic web. [10, 25, 26, 32]

Figure ?? shows the effect of outflow/inflow kinematics, In the ouflow regime photons are blueshifted and the blue part of the line is stronger than the red part. In the inflow regime the opposite effect is carried out, the Ly $\alpha$  phtons are redshifted.



## 1.8 *This Thesis*

In this thesis we study the effect of rotation, an intrinsic characteristic of galaxies, on the morphology of the Lyman  $\alpha$  outcoming profile, to this aim we implement a solid body rotation model in the radiative transfer code CLARA [12]. All the codes used for the analysis of this work is reproducible and public available in [github](#).

### 1.8.1 The importance of modelling the effect of gas bulk rotation

Untill now the effect of rotation have never been studied, and this is an intrinsic property of all galaxies. In this work we study for the first time the effect of galaxy rotation the morphology of the Ly $\alpha$  line.

Modelling the effect of rotation in the morphology of the Ly $\alpha$  line, push further our understanding of the effect of the kinematics of the HII regions on the line. With the knowledge more models into account more realistic analysis can be made in observed Ly $\alpha$  spectra. Now a distinguish between the differents stages of the gas kinematics outflow/inflow, anysotropy Ly $\alpha$  emission, shell cavities and now rotatinal can be made.

Deriving and analytic expression for rotation is also important for the community, computing an analytic solution is more efficient than making all the radiative trasnfer simulation. Radiative transfer codes can be tested against the analytic solution and observed spectra could be easily fitted with the model.

### 1.8.2 Summary of the thesis

A lot of progress has been done in modelling the Ly $\alpha$  line using radiative trasnfer codes. Properties of the gas kinematics such as outflows/inflows. Geometries such as slabs,

spheres, cavities and the propagation of Ly $\alpha$  photons in a clumpy media. Dust effects XX. In this thesis we study the effect of rotation in the morphology of the Ly $\alpha$  profile.

We model a galaxy as an sphere, with an homogeneous mixture of gas and dust. We took the rotation velocity, the optical depth, the viewing angle as free parameters of the model. We also have two different sources of Ly $\alpha$  photons: A central distribution in the galaxy and an homogeneous distribution.

We quantify the effect of rotation with the following characteristics: Escape fraction of Ly $\alpha$  photons, the width of the Ly $\alpha$  line, the average number of scatterings of the Ly $\alpha$  photons and with the position of the Ly $\alpha$  line maxima.

Our main finding is that rotation do have an important effect on the morphology of the Ly $\alpha$  line. Specially in the width of the line and in the position of the maxima. While the average number of scatterings and the scape fraction remain constant.

The line broadens proportional to the rotation velocity, and also the flux in the middle of the line increases with rotation.

The axys of rotation breaks the symmetry of the system, Althogh observers in different viewing angle with respect to the rotation axys observe the same amount of flux of the Ly $\alpha$  profile. This result lead us to find an approximate analytic solution to model rotation.

With these results an approximated analytical solution was derived, taking into the account that the radiative transfer inside de gas cloud is exactly as in the static case. In the sphere surface a Doppler shift due to the difference velocity of an external obsever and the surface have to be taken into account.

### 1.8.3 Future work

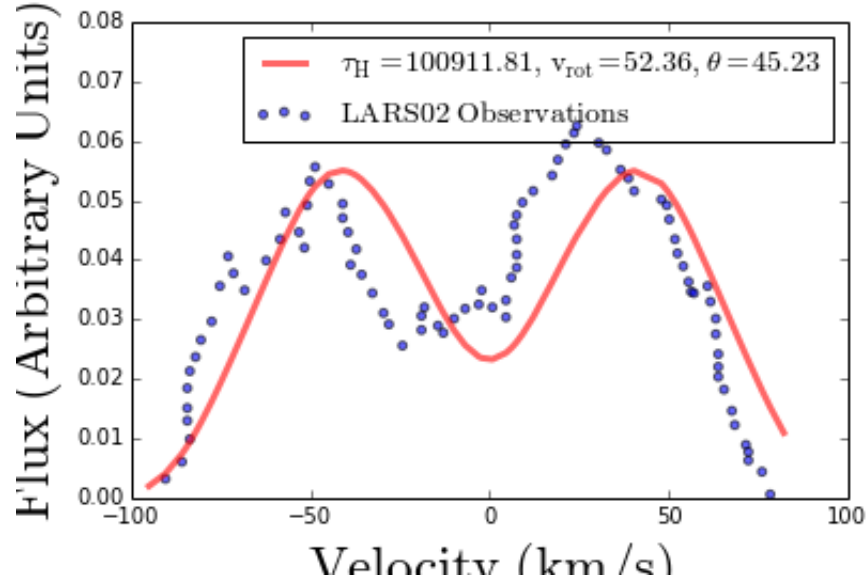
There are two main projects which are based on the results obtained in this work. With the aim of testing our model with observations and improving the kinematic models of the gas by studying two joint effects such as outflows and rotation.

There are LAEs which are governed by rotational movements, also have spherical shapes and the main Ly $\alpha$  sources are in the center. With this propertis such galaxies have the same properties that we studied in this work. Fitting Ly $\alpha$  line profile in order to meassure the rotational velocities of such galaxies would be the direct application and test of our model.

To this aim we are fitting our model using a Marov Chain Monte-Carlo method to the observed nerby galaxy LARS02 [14], a preliminary result is shown in Fig??, this is the



[H]



fit after 20 steps in the Markov chain (a step takes  $\sim 2$  minutes). In the Markov chain we have 3 free parameters  $\tau, v_{rot}$  &  $\theta$  which the best values are represented in the figure.

With this preliminary results we are implementing a MCMC with five free parameters.

Despite the fact that outflows have been broadly studied rotation should also be present on this galaxies. The joint effect of the two above properties should have a direct effect on the morphology of the Lyman  $\alpha$  line. We are combining the effect of rotation followed by an outflow. For the rotation part we are using our analytic solution and for the outflows we are using the shell described in [25].

## Chapter 2

# The effect of gas bulk rotation on the morphology of the Ly $\alpha$ line

J.N. Garavito-Camargo, J.E Forero-Romero & Mark Dijkstra.

### abstract

We present results of radiative transfer calculations to measure the impact of gas bulk rotation on the morphology of the Lyman  $\alpha$  emission line in distant galaxies. We model a galaxy as a sphere with an homogeneous mixture of dust and hydrogen at a constant temperature. These spheres undergo solid-body rotation with maximum velocities in the range  $0-300 \text{ km s}^{-1}$  and neutral hydrogen optical depths in the range  $\tau_{\text{H}} = 10^5-10^7$ . We consider two types of source distributions in the sphere: central and homogeneous. Our main result is that rotation introduces a dependence of the line morphology with viewing angle and rotational velocity. Observations with a line of sight parallel to the rotation axis yield line morphologies similar to the static case. For lines of sight perpendicular to the rotation axis both the intensity at the line center and the line width increase with rotational velocity. Along the same line of sight, the line becomes single peaked at rotational velocities close to half the line width in the static case. Notably, we find that rotation does not induce any spatial anisotropy in the integrated line flux, the escape fraction or the average number of scatterings. This is because Lyman  $\alpha$  scattering through a rotating solid-body proceeds identical as in the static case. The only difference is the doppler shift from the different regions in the sphere that move with respect to the observer. This allows us to derive an analytic approximation for the viewing-angle dependence of the emerging spectrum, as a function of rotational velocity.

## 2.1 Introduction

The detection of strong Ly $\alpha$  emission lines has become an essential method in extragalactic astronomy to find distant star-forming galaxies [1, 33–39]. The galaxies detected using this method receive the name of Ly $\alpha$  emitters (LAEs). A detailed examination of this galaxy population has diverse implications for galaxy formation, reionization and the large scale structure of the Universe. Attempts to fully exploit the physical information included in the Ly $\alpha$  line require an understanding of all the physical factors involved in shaping the line. Due to the resonant nature of this line, these physical factors notably include temperature, density and bulk velocity field of the neutral Hydrogen in the emitting galaxy and its surroundings. A basic understanding of the quantitative behavior of the Ly $\alpha$  line has been reached through analytic studies in the case of a static configurations, such as uniform slabs [3–5] and uniform spheres [24]. Analytic studies of configurations including some kind of bulk flow only include the case of a sphere with a Hubble like expansion flow [40]. A more detailed quantitative description of the Ly $\alpha$  line has been reached through Monte Carlo (MC) simulations [3, 41, 42]. In the last two decades these studies have become popular due to the availability of computing power. Early into the 21st century, the first studies focused on homogeneous and static media [43–45]. Later on, the effects of clumpy media [28] and expanding/contracting shell/spherical geometries started to be studied [11, 24, 27]. For a recent review, we refer the interested reader to Dijkstra [16]. Similar codes have applied these results to semi-analytic models of galaxy formation [46, 47] and results of large hydrodynamic simulations [12, 31, 48]. Recently, Monte Carlo codes have also been applied to the results of high resolution hydrodynamic simulations of individual galaxies [10, 25, 26, 32]. Meanwhile, recent developments have been focused on the systematic study of clumpy outflows [9] and anisotropic velocity configurations [29]. The recent studies of galaxies in hydrodynamic simulations [10, 25, 26, 32] have all shown systematic variations in the Ly $\alpha$  line with the viewing angle. These variations are a complex superposition of anisotropic density configurations (i.e. edge-on vs. face-on view of a galaxy), the inflows observed by gas cooling and the outflows included in the supernova feedback process of the simulation. These bulk flows physically correspond to the circumgalactic and intergalactic medium (CGM and IGM). These effects are starting to be studied in simplified configurations that vary the density and wind characteristics [29, 30]. However, in all these efforts the effect of rotation, which is an ubiquitous feature in galaxies, has not been systematically studied. The processing of the Ly $\alpha$  photons in a rotating interstellar medium (ISM) must have some kind of impact in the Ly $\alpha$  line morphology. Performing that study is the main goal of this paper. We investigate for the first time the impact of rotation on the morphology of the Ly $\alpha$  line. We focus on a simplified system: a spherical gas cloud with homogeneous density and solid body rotation, to study the line

morphology and the escape fraction in the presence of dust. We base our work on two independent Monte Carlo based radiative transfer codes presented in [12] and [9]. This paper is structured as follows: In §2.2 we present the implementation of bulk rotation into the Monte Carlo codes, paying special attention to coordinate definitions. We also present a short review of how the Ly $\alpha$  radiative transfer codes work and list the different physical parameters in the simulated grid of models. In §2.3 we present the results of the simulations, with special detail to quantities that show a clear evolution as a function of the sphere rotational velocity. In §2.4 we discuss the implications of our results. In the last section we present our conclusions. The Appendix presents the derivation of an analytic expression to interpret the main trends observed in the Monte Carlo simulations. In this paper we express a photon's frequency in terms of the dimensionless variable  $x \equiv (\nu - \nu_\alpha)/\Delta\nu_D$ , where  $\nu_\alpha = 2.46 \times 10^{15}$  Hz is the Ly $\alpha$  resonance frequency,  $\Delta\nu_D \equiv \nu_\alpha \sqrt{2kT/m_p c^2} \equiv \nu_\alpha v_{\text{th}}/c$  is the Doppler broadening of the line which depends on the neutral gas temperature  $T$  or equivalently the thermal velocity  $v_{\text{th}}$  of the atoms. We also use the parameter  $a$  to define the relative line width as  $a = \Delta\nu_\alpha/2\Delta\nu_D$ , where  $\Delta\nu_\alpha$  is the intrinsic linewidth. For the temperature  $T = 10^4$ K used in our radiative transfer calculations the thermal velocity is  $v_{\text{th}} = 12.8 \text{ km s}^{-1}$ .

## 2.2 Models of bulk gas rotation

Describing the kinematics of gas rotation in all generality is a complex task, specially at high redshift where there is still missing a thorough observational account of rotation in galaxies beyond  $z > 1.0$ . Even at low redshifts there is a great variation in the shape of the rotation curve as observed in HI emission as a function of the distance to the galaxy center. However there are two recurrent features. First, in the central galactic region the velocity increases proportional to the radius, following a solid rotation behavior. Second, beyond a certain radius the rotation curve tends to flatten. An ab-initio description of such realistic rotation curves in simulations depends on having access to the dynamic evolution of all mass components in the galaxy: stars, gas and dark matter. Such level of realism is extremely complex to achieve, specially if one wants to get a systematic description based on statistics of simulated objects. Following the tradition of studies of Ly $\alpha$  emitting systems, we implement a model with simplified geometry. We assume that the gas is homogeneously distributed in a sphere that rotates as a solid body with constant angular velocity. This simple model will contain only one free parameter: the linear velocity at the sphere's surface,  $V_{\text{max}}$ .

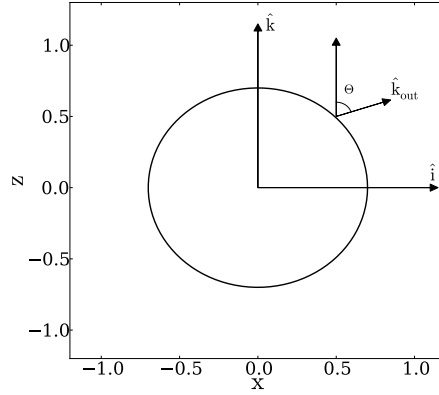


FIGURE 2.1: Geometry of the gas distribution. The angular velocity vector is parallel to the unit vector  $\hat{k}$ . In order to describe the departures from spherical symmetry we use the polar angle  $\theta$  formed by the direction of the outgoing photons with respect to the  $z$ -axis. We define the variable  $\mu \equiv \cos \theta$  to report to present our results. Computing the spectra for photons in a narrow range of  $\mu$  is equivalent to having a line-of-sight oriented in that direction.

### 2.2.1 Detailed Implementation of Rotation

In the Monte Carlo code we define a Cartesian coordinate system to describe the position of each photon. The origin of this system coincides with the center of the sphere and the rotation axis is defined to be  $z$ -axis. With this choice, the components of the gas bulk velocity field,  $\vec{v} = v_x \hat{i} + v_y \hat{j} + v_z \hat{k}$ , can be written as

$$v_x = -\frac{y}{R} V_{\max}, \quad (2.1)$$

$$v_y = \frac{x}{R} V_{\max}, \quad (2.2)$$

$$v_z = 0, \quad (2.3)$$

where  $R$  is the radius of the sphere and  $V_{\max}$  is the linear velocity at the sphere's surface. The minus/plus sign in the  $x/y$ -component of the velocity indicates the direction of rotation. In this case we take the angular velocity in the same direction as the  $\hat{k}$  unit vector. With these definitions we can write the norm of the angular velocity as  $\omega = V_{\max}/R$ . For each photon in the simulation we have its initial position inside the sphere, direction of propagation  $\hat{k}_{\text{in}}$  and reduced frequency  $x_{\text{in}}$ . The photon's propagation stops once they cross the surface of the sphere. At this point we store the position, the outgoing direction of propagation  $\hat{k}_{\text{out}}$  and the reduced frequency  $x_{\text{out}}$ . We now define the angle  $\theta$  by  $\cos \theta = \hat{k}_{\text{out}} \cdot \hat{k} \equiv \mu$ , it is the angle of the outgoing photons with respect to the direction of the angular velocity. We use the variable  $\mu$  to study the anisotropy induced by rotation. Fig. 2.1 shows the geometry of the problem and the important variables.

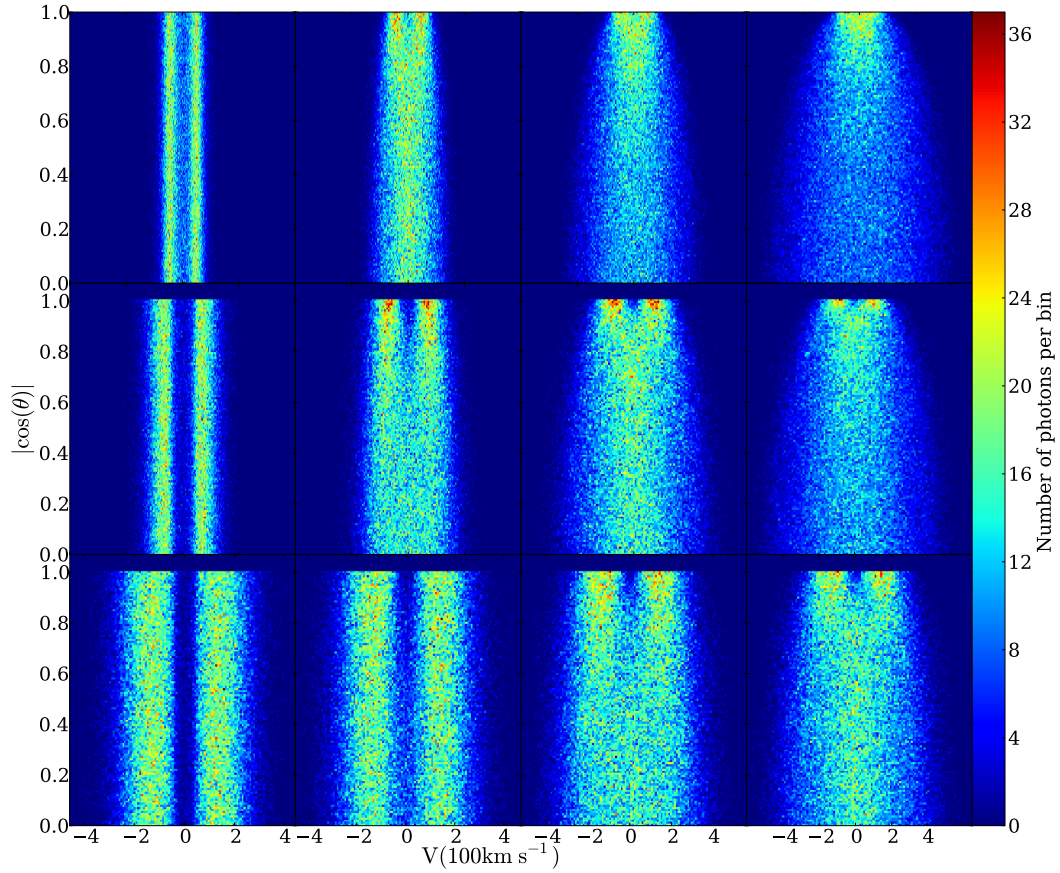


FIGURE 2.2: 2D histogram showing the number of photons that escape with frequency  $x$  forming an angle  $\theta$  (parametrized as  $|\cos \theta|$ ) with the rotation axis. The rotational velocity ( $0, 100, 200, 300 \text{ km s}^{-1}$ ) increases from left to right and the optical depth ( $10^5, 10^6, 10^7$ ) from top to bottom. The Ly $\alpha$  photons are initialized at the center of the sphere. Two main results can be read from this figure. First, the line morphology depends on the viewing angle. Second, the line can become single peaked for high rotational velocities.

### 2.2.2 Brief Description of the Radiative Transfer Codes

Here we briefly describe the relevant characteristics of the two radiative transfer codes we have used. For a detailed description we refer the reader to the original papers [12] and [9]. The codes follow the individual scatterings of Ly $\alpha$  photons as they travel through a 3D distribution of neutral Hydrogen. The frequency of the photon (in the laboratory frame) and its direction of propagation change at every scattering. This change in frequency is due to the peculiar velocities of the Hydrogen absorbing and re-emitting the photon. Once the photons escape the gas distribution we store their direction of propagation and frequency at their last scattering. The initialization process for the Ly $\alpha$  photons specifies its position, frequency and direction of propagation. We select the initial frequency to be exactly the Ly $\alpha$  rest-frame frequency in the gas reference frame and the direction of propagation to be random following an flat probability distribution

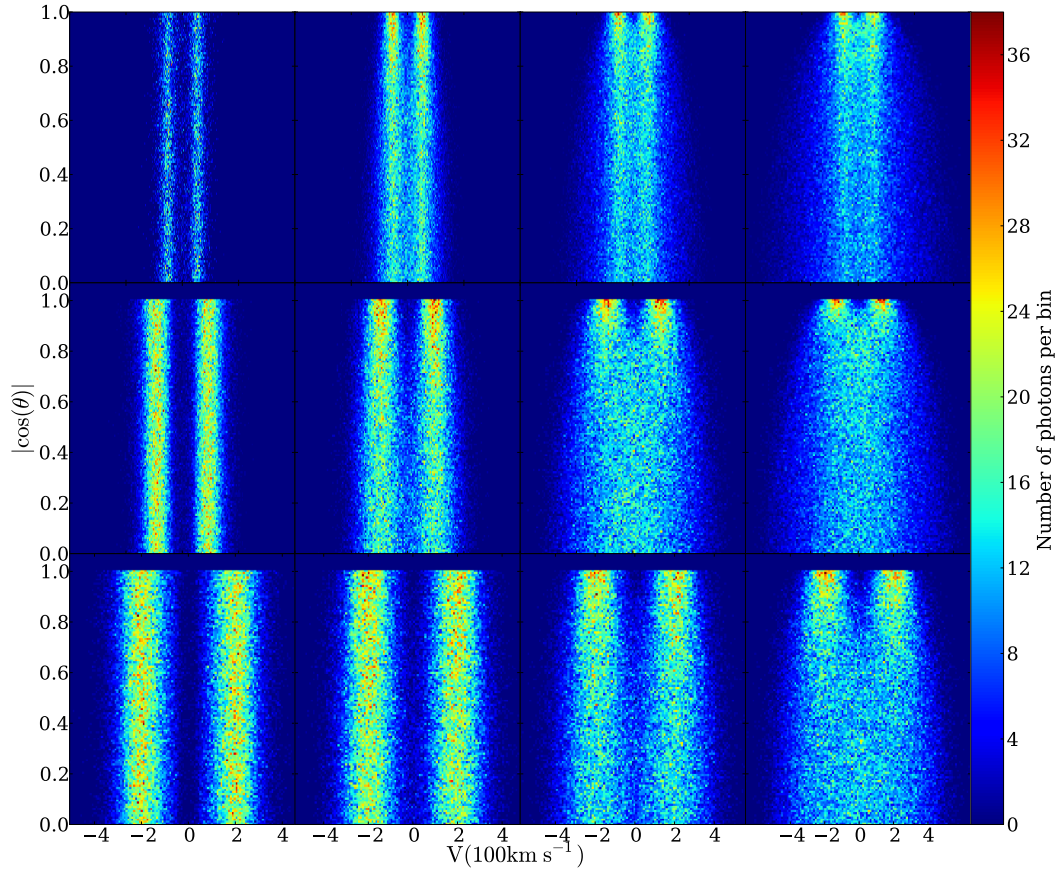


FIGURE 2.3: Same as Fig. 2.2 for Ly $\alpha$  photons initialized homogeneously throughout the sphere.

over the sphere. It means that for photons emitted from the center of the sphere  $x_{\text{in}} = 0$ , while photons emitted at some radii with a peculiar velocity  $\vec{v}$  have initial values  $x_{\text{in}}$  depending on its direction of propagation:  $x_{\text{in}} = \vec{v} \cdot \hat{k}_{\text{in}} / v_{\text{th}}$ . We do not include the effect of turbulent velocities in the initialization. We neglect this given that the induced perturbation should be on the close to the thermal velocity,  $12.8 \text{ km s}^{-1}$ , which is one order of magnitude smaller than the velocity widths ( $100\text{-}500 \text{ km s}^{-1}$ ) in the static case. If dust is present, the photon can interact either with a Hydrogen atom or dust grain. In the case of a dust interaction the photon can be either absorbed or scattered. This probability is encoded in the dust albedo,  $A$ , which we chose to be  $1/2$ . In order to obtain accurate values for the escape fraction of photons in the presence of dust, we do not use any accelerating mechanism in the radiative transfer. The codes treat the gas as homogeneous in density and temperature. This implies that the gas is completely defined by its geometry (i.e. sphere or slab), temperature  $T$ , Hydrogen optical depth  $\tau_{\text{H}}$ , dust optical depth  $\tau_{\text{a}}$  and the bulk velocity field  $\vec{v}$ .



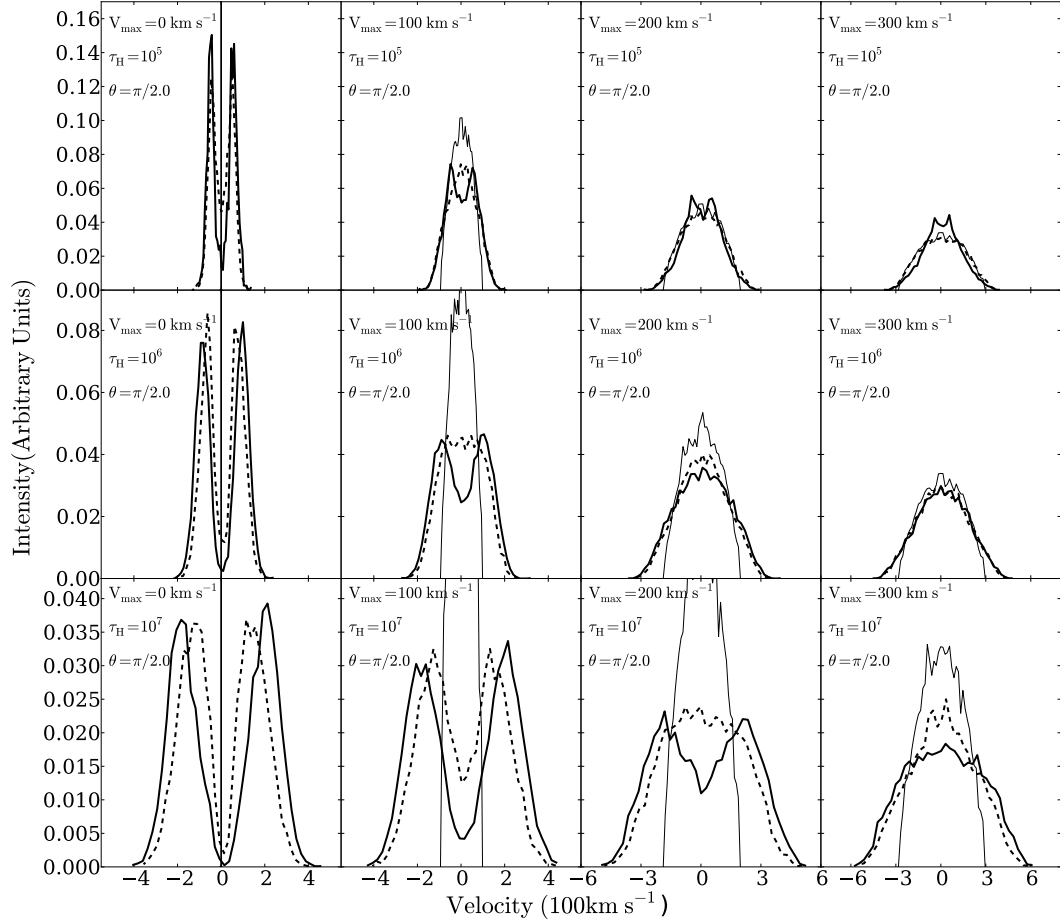


FIGURE 2.4: Shape of the Ly $\alpha$  line for different maximum rotational velocities for a LoS perpendicular to the rotation axis ( $|\mu| \sim 0$ ). The continuous (dashed) line represents the central (homogeneous) source distributions. The continuous thin line represents the intrinsic homogeneous spectrum. The panels follow the same distribution as in Figs 2.2 and 2.3.

### 2.2.3 Grid of Simulated Galaxies

In the Monte Carlo calculations we follow the propagation of  $N_\gamma = 10^5$  numerical photons through different spherical galaxies. For each galaxy we vary at least one of the following parameters: the maximum rotational velocity  $V_{\max}$ , the hydrogen optical depth  $\tau_H$ , the dust optical depth  $\tau_a$  and the initial distribution of photons with respect to the gas. In total there are 48 different models combining all the possible different variations in the input parameters. Table 2.1 lists the different parameters we used to generate the models. The results and trends we report are observed in both Monte Carlo codes.



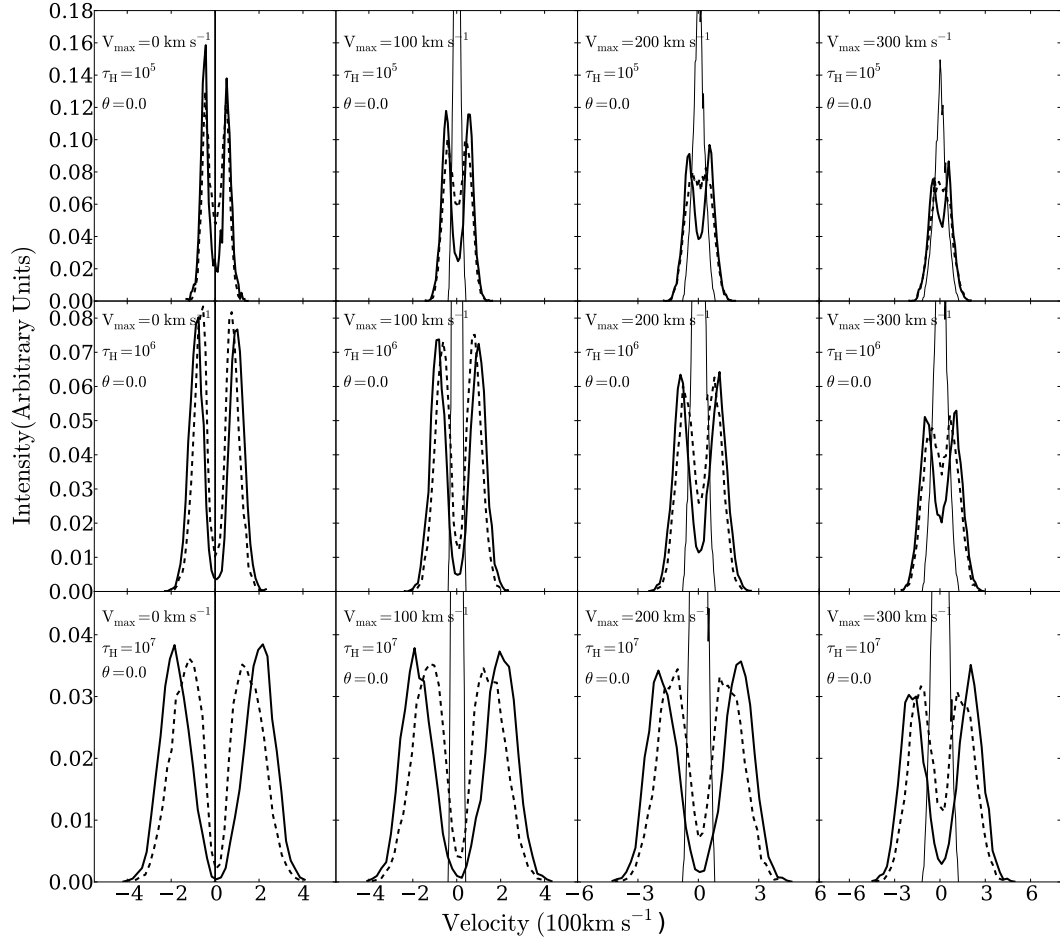


FIGURE 2.5: Shape of the Ly $\alpha$  line for different maximum rotational velocities for a LoS perpendicular to the rotation axis ( $|\mu| \sim 1$ ). The continuous (dashed) line represents the central (homogeneous) source distributions. The continuous thin line represent the intrinsic homogeneous spectrum. The panels follow the same distribution as in Figs 2.2 and 2.3.

Physical Parameter (units)	Symbol	Values
Velocity ( $\text{km s}^{-1}$ )	$V_{\text{max}}$	0, 100, 200, 300
Hydrogen Optical Depth	$\tau_H$	$10^5, 10^6, 10^7$
Dust Optical Depth	$\tau_a$	0,1
Photons Distributions		Central, Homogeneous

TABLE 2.1: Summary of Physical Parameters of our Monte Carlo Simulations.

## 2.3 Results

The main results of this paper are summarized in Fig. 2.2 and 2.3. They show 2D histograms of the escape frequency  $x$  and outgoing angle  $\theta$  parametrized by  $|\mu|$ . Taking into account only photons around a value of  $|\mu|$  gives us the emission detected by an observer located at an angle  $\theta$  with respect to the rotation axis. We have verified that the solutions are indeed symmetric with respect to  $\mu = 0$ . We have also verified that the total flux is the same for all  $\mu$ . From these figures we can see that the line properties change with rotational velocity and depend on the viewing angle  $\theta$ . In the next subsections we quantify the morphology changes with velocity, optical depth and viewing angle. We characterize the line morphology by its total intensity, the full width at half maximum, (FWHM) and the location of the peak maxima. In order to interpret the morphological changes in the line we also report the median number of scatter for each Ly $\alpha$  photon in the simulation. For the models where dust is included we measure the escape fraction as a function of rotational velocity and viewing angle.

### 2.3.1 Line Morphology

The first column in both Fig. 2.2 and 2.3 shows that for the static sphere the line properties are independent of  $|\mu|$ , as it is expected due to the spherical symmetry. However, for increasing rotational velocities, at a fixed optical depth, there are clear signs that this symmetry is broken. If the viewing angle is aligned with the rotation axis,  $|\mu| \sim 1$ , the Ly $\alpha$  line keeps a double peak with minor changes in the morphology as the rotational velocity increases. However, for a line of sight perpendicular to the rotation axis,  $|\mu| \sim 0$ , the impact of rotation is larger. The double peak readily transforms into a single peak. This is clear in Fig. 2.4 and in Fig. 2.5 where we present the different line morphologies for  $|\mu| \sim 0$  and  $|\mu| \sim 1$  for the homogeneous and central configurations. The panels have the same distribution as Fig. 2.2 and 2.3. There are three clear effects on the line morphology as the rotational velocity increases. First, the line broadens; second, the double peaks reduce their intensity; and third, the intensity at the line centre rises. The last two effects are combined to give the impression that the double peaks are merged into a single one at high rotational velocities.

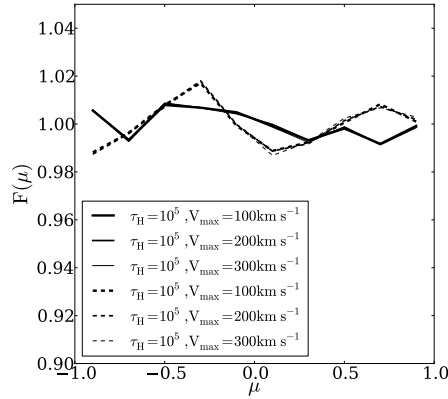


FIGURE 2.6: Integrated flux distribution as a function of the viewing angle as parametrized by  $\mu$ . Continuous (dashed) correspond to central (homogeneous) source distribution. The models correspond to an optical depth of  $\tau_H = 10^5$  and rotational velocities of  $100 \text{ km s}^{-1}$ ,  $200 \text{ km s}^{-1}$  and  $300 \text{ km s}^{-1}$ . The distributions are flat in the range of models probed in this paper, meaning that the integrated flux for all viewing angles is the same.

### 2.3.2 Integrated Line Intensity

We now consider possible variations in the integrated flux with respect to the viewing angle  $\theta$ . To this end we define the normalized flux seen by an observer at an angle  $\mu$  by:

$$F(\mu) = \frac{2\Delta N}{N\Delta\mu}, \quad (2.4)$$

where  $\mu = \cos\theta$ ,  $N$  is the total number of outgoing photons,  $\Delta N$  is the number of photons in an angular bin  $\Delta\theta$ . This definition satisfies the condition  $\int_{-1}^1 F(\mu)d\mu/2 = 1$ . In the case of perfect spherical symmetry one expects a flat distribution with  $F(\mu) = 1$ . Fig. 2.6 shows the results for a selection of models with  $\tau_H = 10^5$ , different rotational velocities and the two types of source distributions. This shows that  $F(\mu)$  is consistent with being flat, apart from some statistical fluctuations on the order of 2%. This is a remarkable result: while the rotation axis defines preferential direction, the integrated flux is the same for all viewing angles in the range of parameters explored in this paper. This can be understood from the fact that *radiative transfer inside a sphere that undergoes solid-body rotation proceeds identical as inside a static sphere*: we can draw a line between any two atoms within the rotating cloud, and their relative velocity along this line is zero (apart from the relative velocity as a result of random thermal motion), irrespective of the rotation velocity of the cloud. This relative velocity is what is relevant for the radiative transfer<sup>1</sup>

<sup>1</sup>This point can be further illustrated by considering the path of individual photons: let a photon be emitted at line center ( $x = 0$ ), in some random direction  $\mathbf{k}$ , propagate a distance that corresponds to  $\tau_0 = 1$ , scatter fully coherently (i.e.  $x = 0$  after scattering in the gas frame) by  $90^\circ$ , and again propagate a distance that corresponds to  $\tau_0 = 1$ . The position where the photon scatters next does *not* depend on the rotation of the cloud, nor on  $\mathbf{k}$ .

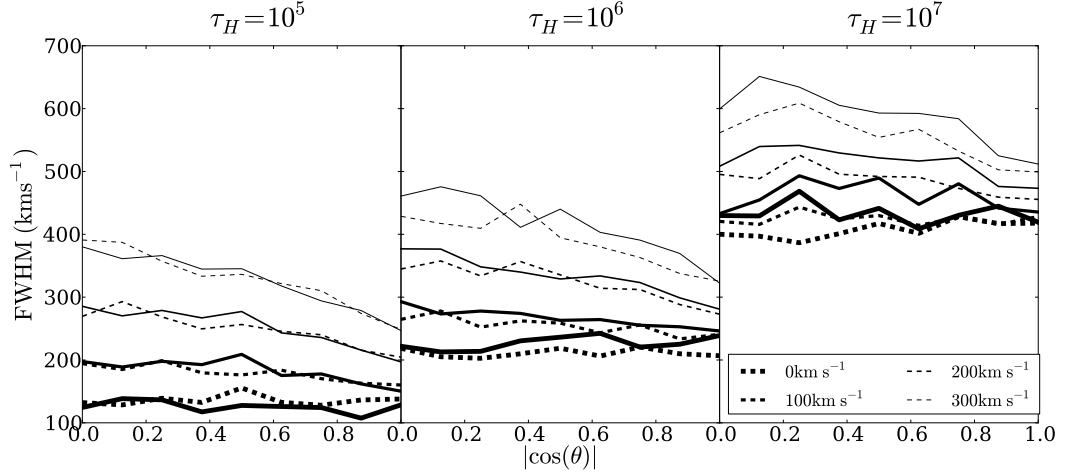


FIGURE 2.7: FWHM for the non-dusty models as a function of the viewing angle parametrized by  $|\cos \theta|$ . Continuous (dashed) lines correspond to central (homogeneous) source distributions. The general trend is of an decreasing line width as the line of sight becomes parallel to the rotation axis.

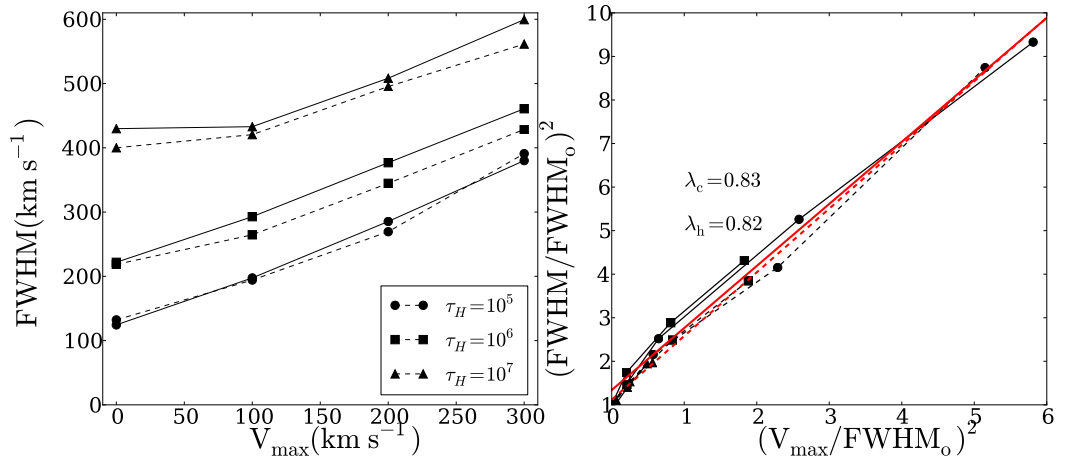


FIGURE 2.8: FWHM for the non-dusty models as a function of rotational velocity  $V_{\max}$  for observers located perpendicular to the rotation axis. The left panel shows the results in velocity units while the right panel normalizes the data by the FWHM in the static case. Continuous (dashed) lines correspond to central (homogeneous) source distributions. The straight lines represent the fit to the data using the expression in Eq. (2.5).

### 2.3.3 Full Width at Half Maximum

We use the full width at half maximum (FWHM) to quantify the line broadening. We measure this width from the line intensity histogram by finding the values of the velocities at half maximum intensity. We use lineal interpolation between histogram points to get a value more precise than the bin size used to construct the histogram. Fig. 2.7 shows the FWHM for all models as a function of the viewing angle. The FWHM increases for decreasing values of  $\mu$  (movement from the poles to the equator) and increasing values of

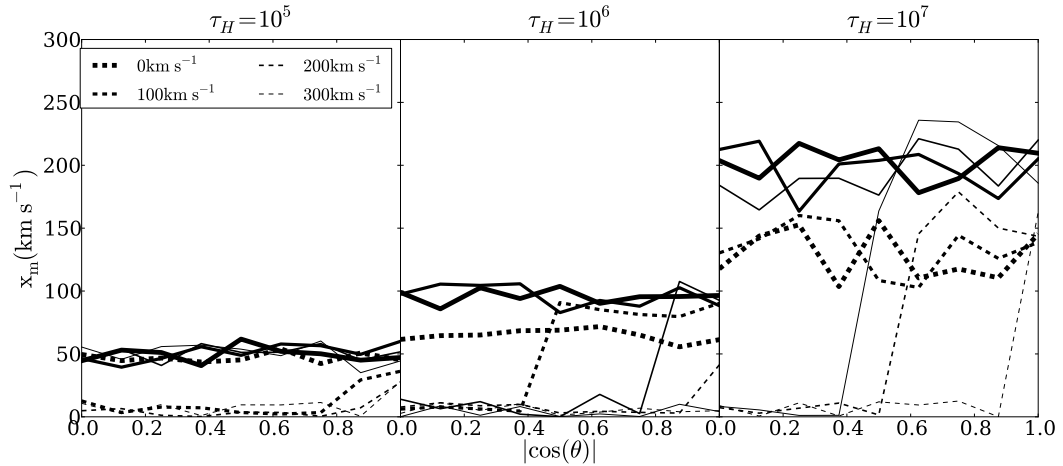


FIGURE 2.9: Position of the line maxima as a function of maximum rotational velocity  $V_{\max}$ . Continuous (dashed) lines correspond to central (homogeneous) source distributions. A value of  $x_{\max} = 0$  indicates that line becomes single peaked.

$V_{\max}$ . In Fig. 2.8 we fix  $|\mu| < 0.1$ , i.e. viewing angle perpendicular to the rotation axis, to plot the FWHM as a function of rotational velocity. We parametrize the dependency of the line width with  $V_{\max}$  as

$$\text{FWHM}^2 = \text{FWHM}_0^2 + V_{\max}^2/\lambda^2, \quad (2.5)$$

where  $\text{FWHM}_0$  is the velocity width in the static case and  $\lambda$  is a positive scalar to be determined as a fit to the data. With this test we want to know to what extent the new velocity width can be expressed as a quadratic sum of the two relevant velocities in the problem. All the models fall into a single family of lines in the plane shown in the right panel of Fig. 2.8, justifying the choice of our parametrization. We fit simultaneously all the points in two separate groups, central and homogeneous sources. We find that these values are  $\lambda_c = 0.83 \pm 0.06$  and  $\lambda_h = 0.82 \pm 0.05$  respectively.

### 2.3.4 Line Maxima

We measure the peak maxima position,  $x_m$ , to quantify the transition from double into single peak profiles. In Fig. 2.9 we show the dependence of  $x_m$  with the viewing angle parametrized by  $|\cos\theta|$  for different rotational velocities. There are two interesting features that deserve attention. First, for a viewing angle parallel to the rotational axis ( $\mu \sim 1.0$ ) the maxima of all models with the same kind of source initialization are similar regardless of the rotational velocity. Second, at a viewing angle perpendicular to the rotation axis ( $\mu \sim 0.0$ ) a large fraction of models become single peaked. This

Source Distribution	$\tau_H$	$V_{\max}$ (km s $^{-1}$ )			
		0	100	200	300
Homogeneous	$10^5$	0.263	0.263	0.263	0.263
	$10^6$	0.291	0.292	0.293	0.293
	$10^7$	0.228	0.228	0.228	0.228
Central	$10^5$	0.096	0.096	0.096	0.096
	$10^6$	0.066	0.066	0.066	0.066
	$10^7$	0.015	0.016	0.016	0.015

TABLE 2.2: Escape fraction values for all dusty models.

feature appears more frequently for homogeneously distributed sources if all the other parameters are equal.

### 2.3.5 Dusty Clouds: Escape Fraction

We now estimate the escape fraction  $f_{\text{esc}}$  for the dusty models. The main result is that we do not find any significant dependence with either the viewing angle nor the rotational velocity. This is consistent with our finding in § 2.3.2, that radiative transfer inside the cloud does not depend on its rotational velocity. For completeness we list in Table 2.2 the escape fraction for all models. We now put these results in the context of the analytic solution for the infinite slab[5]. In Neufeld’s set-up the analytic solution depends uniquely on the product  $(a\tau_H)^{1/3}\tau_A$  where  $\tau_A = (1 - A)\tau_a$ , valid only in the limit  $a\tau_H \gg 1$ . At fixed values of  $\tau_a$  the escape fraction monotonically decreases with increasing values of  $\tau_H$ . This expectation holds for the central sources. But in the case of homogeneous sources the escape fraction increases slightly from  $\tau_H = 10^5$  to  $\tau_H = 10^6$ . The naive interpretation of the analytic solution does not seem to hold for photons emitted far from the sphere’s center. We suggest that increasing  $\tau_H$  from  $10^5$  to  $10^6$  causes a transition from the ‘optically thick’ to the ‘extremely optically thick’ regime for a noticeable fraction of the photons in the homogeneous source distribution. In the optically thick regime, Ly $\alpha$  photons can escape in ‘single flight’ which corresponds to a scenario in which the photon resonantly scatters  $10^4 - 10^5$  times until it is scattered into the wing of the line ( $x \sim 3 - 4$ ). At these frequencies the medium is optically thin, and the photons can escape efficiently in a single flight. In contrast, in an extremely optically thick medium Ly $\alpha$  photons escape in a ‘single excursion’ [3]. Here, photons that are scattered into the wing of the line escape from the medium in a sequence of wing scattering events. In both cases, Ly $\alpha$  photons resonantly scatter  $10^4$ - $10^5$  times. Because we keep our clouds the same size, the mean free path of Ly $\alpha$  photons that scatter resonantly is 10 times larger for the case  $\tau_H = 10^5$  than for  $\tau_H = 10^6$ . If we

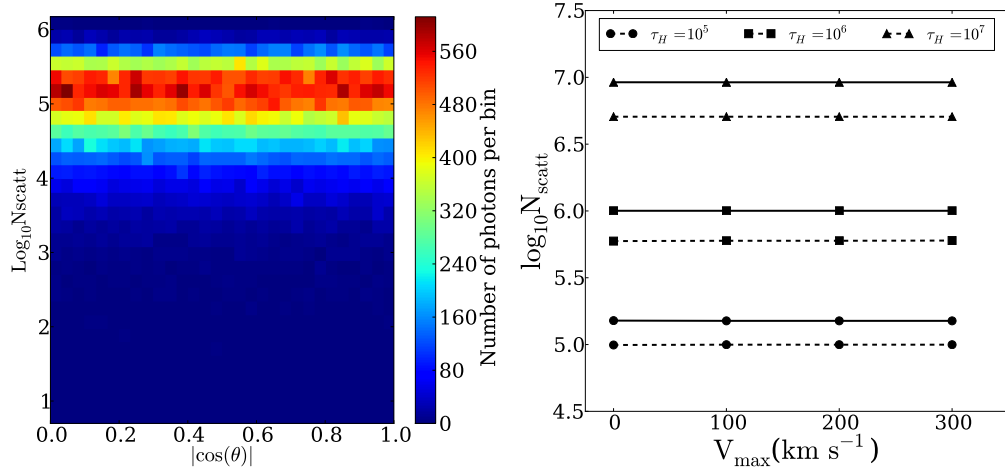


FIGURE 2.10: 2D histogram of the logarithm of the average number of scatterings as function of  $\mu$  (left) and the maximum rotational velocity  $V_{\text{max}}$  (right). The left panel shows the behaviour for  $\tau = 10^5$  and  $V_{\text{max}} = 300 \text{ km s}^{-1}$  as a function of  $|\cos \theta|$ , the color indicates the number of photons per bin. In the right panel the continuous (dashed) lines represent the results for the central (homogeneous) model. The independence of  $N_{\text{scatt}}$  with  $\mu$  and  $V_{\text{max}}$  is present in all models.

compute the average distance  $D$  travelled by Ly $\alpha$  photons through a medium of size  $R$  as a function of line center optical depth  $\tau_H$ , then we find that during the transition from optically thick to extremely optically thick the mean traversed distance  $D$  actually decreases slightly. This decrease is unique to this transition region, and  $D$  generally increases with  $\tau_H$  at other values of  $\tau_H$ .

### 2.3.6 Average Number of Scatterings

The number of scatterings affects the escape frequency of a Ly $\alpha$  photon. Studying this quantity further illustrates the independence of the integrated flux and the escape fraction on rotational velocity. In Fig. 2.10 we show the average number of scatterings  $\langle N_{\text{scatt}} \rangle$  as a function of the cosine of the outgoing angle  $|\cos \theta|$  and the rotational velocity  $V_{\text{max}}$ . From the right panel observe that the number of scatterings and the outgoing angle are independent. This plot corresponds to the specific case of the central model with  $\tau = 10^5$  and  $V_{\text{max}} = 300 \text{ km s}^{-1}$ , but we have verified that this holds for all models. The right panel of Fig. 2.10 shows how the average number of scatterings is also independent from the rotational velocity. The lower number of average scatterings in the homogeneous source distribution is due to a purely geometrical effect. Photons emitted close to the surface go through less scatterings before escaping. In static configurations it is expected that the optical depth correlates number of scatterings. This has been precisely quantified in the case of static infinite slab. In that model for centrally emitted sources the average number of scatterings depends only on the optical depth  $\langle N_{\text{scatt}} \rangle =$

$1.612\tau_H$  [3, 4], for homogeneously distributed sources  $\langle N_{\text{scatt}} \rangle = 1.16\tau_H$  [4]. In our case we find that for the central model the number of scatterings is proportional to the optical depth, with  $\langle N_{\text{scatt}} \rangle = (1.50, 1.00, 0.92)\tau_H$  for optical depth values of  $\tau_H = (10^5, 10^6, 10^7)$  respectively. For the homogeneous sources we find that  $\langle N_{\text{scatt}} \rangle = (0.99, 0.59, 0.51)\tau_H$ .

## 2.4 Discussion

### 2.4.1 Towards an analytical description

There is a key result of our simulations that allows us to build an analytical description for the outgoing spectra. It is the independence of the following three quantities with the rotational velocity and the viewing angle: integrated flux, average number of scatterings and escape fraction. As we explained in § 2.3.2, the best way to understand this is that radiative transfer inside a sphere that undergoes solid-body rotation proceeds identical to that inside a non-rotating sphere. While scattering events off atoms within the rotating cloud impart Doppler boosts on the Ly $\alpha$  photon, these Doppler boost are only there in the lab-frame. Therefore, in the frame of the rotating gas cloud all atoms are stationary with respect to each other and the scattering process proceeds identical as in the static case (also see § 2.3.2 for an additional more quantitative explanation). This result allows us to analytically estimate the spectrum emerging from a rotating cloud: The spectrum of Lyman  $\alpha$  photons emerging from a rotating gas cloud is identical as for the static case in a frame that is co-rotating with the cloud. However, the surface of cloud now moves in the lab-frame. Each surface-element on the rotating cloud now has a bulk velocity with respect to a distant observer. In order to compute the spectrum one can integrate over all the surface elements in the sphere with their corresponding shift in velocity and an additional weight by the surface intensity. Fig 2.11 shows some examples of analytic versus full MC spectra using this approach (the implementation details are in the Appendix). The left panel shows the results for different rotational velocities in the case of  $\tau_H = 10^7$  and an observer located perpendicular to the axis of rotation ( $i = 0$  in the scheme of Fig A.1 in the Appendix). The right panel shows the results for different viewing angles in the case of  $\tau_H = 10^7$  and a rotational velocity of  $V_{\text{max}} = 300 \text{ km s}^{-1}$ . The two methods clearly give good agreement, though not perfect. In particular, the left panel shows that the MC gives rise to a spectrum that is slightly more concentrated towards the line centre. As we explain in Appendix A, we do not expect perfect agreement, because this requires an analytic solution for the spectrum of Ly $\alpha$  photons emerging from a static, optically extremely thick cloud *as a function of the angle at which they escape from the sphere*. This solution does not exist in the literature. It is possible to get better agreement by modifying the surface brightness



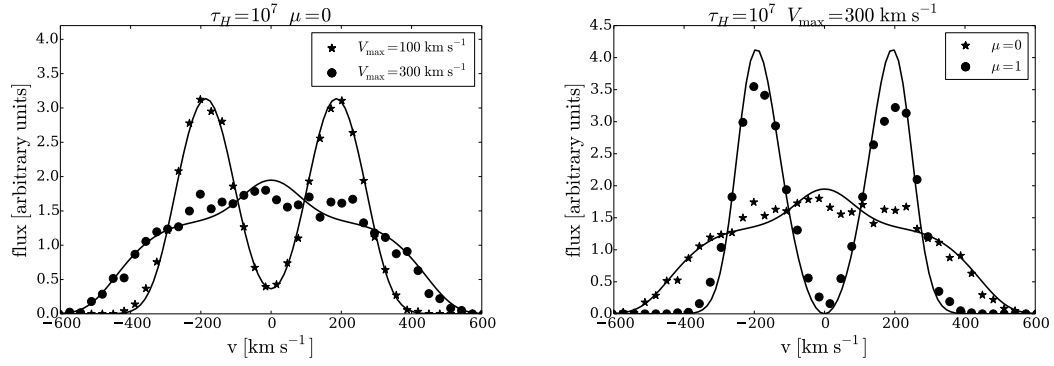


FIGURE 2.11: Comparison of the Monte Carlo results against the analytic solution. The left panel explores the results of different velocities. The right panel presents the results for two different observers: parallel and perpendicular to the rotational axis,  $\mu = 1$  and  $\mu = 0$  respectively.

profile. In any case, the analytic calculation closely captures the results obtained from the full calculations from the MC simulations. As such, they are extremely useful and provide us with a quick tool to verify our calculations at the first order level.

#### 2.4.2 Impact on the interpretation of simulated and observational data

We now compare our findings to other computational results and discuss its possible implications for the interpretation of observational data. **Escape at Line Center.** Our models have shown that rotation enhances the flux density at line center (see Fig. 2.4). It has recently been proposed that galaxies with Ly $\alpha$  spectral lines that contain flux at line center may be ‘leaking’ ionizing (LyC) photons [30, 49]. The main reason for this possible connection is that the escape of ionizing (LyC) photons requires  $N_{\text{HI}} < 10^{17} \text{ cm}^{-2}$ . The same low column densities facilitate the escape of Ly $\alpha$  photons at (or close to) line center. Our work suggests that rotation may provide an alternative explanation. **Single peaked lines.** The presence of single peaked profiles has been associated to inflow/outflow dynamics [9, 11]. Gas bulk rotation can also be considered as a probable origin for that behaviour, provided that the observed single peak is highly symmetric. Similarly, in the case of double peaked lines with a high level of flux at the line center, rotation also deserves to be considered in the pool of possible bulk flows responsible for that feature, specially if the two peaks have similar intensities. **Systemic velocities.** There are observational measurements for the velocity shift between the Ly $\alpha$  and other emission lines. In our study we find that the position of the peak maxima can suddenly change with rotation and viewing angle. Namely the line can become single peaked for high rotational velocities and viewing angles perpendicular to the rotation axis. **Galaxy simulations with gas rotation.** [25] studied Ly $\alpha$  line emission in two high resolution

simulations of individual galaxies. The main purpose of their study was to assess the impact of two different ISM prescriptions. However, each simulated galaxy had a disc structure with a clear rotation pattern in the ISM and inflowing gas from the circumgalactic region. The configuration had an axial symmetry and they reported a strong dependence of both the escape fraction and the total line intensity as a function of the  $\theta$  angle. From our study, none of these two quantities has a dependence either on the inclination angle or the rotational velocity. We suggest that the effect reported by [25] is consistent with being a consequence of the different hydrogen optical depth for different viewing angles and not as an effect of the bulk rotation. **Zero impact on the Ly $\alpha$  escape fraction.** Study of high redshift LAEs in numerical simulation often requires the estimation of the Ly $\alpha$  escape fraction in order to compare their results against observations [12, 31, 46, 47, 50]. Most of these models estimate the escape fraction from the column density of dust and neutral Hydrogen. The results of our simulation indicate that the rotational velocity does not induce additional uncertainties in those estimates.

## 2.5 Conclusions

In this paper we quantified for the first time in the literature the effects of gas bulk rotation in the morphology of the Ly $\alpha$  emission line in star forming galaxies. Our results are based on the study of an homogeneous sphere of gas with solid body rotation. We explore a range of models by varying the rotational speed, hydrogen optical depth, dust optical depth and initial distribution of Ly $\alpha$  photons with respect to the gas density. As a cross-validation, we obtained our results from two independently developed Monte-Carlo radiative transfer codes. Two conclusions stand out from our study. First, rotation clearly impacts the Ly $\alpha$  line morphology; the width and the relative intensity of the center of the line and its peaks are affected. Second, rotation introduces an anisotropy for different viewing angles. For viewing angles close to the poles the line is double peaked and it makes a transition to a single peaked line for high rotational velocities and viewing angles along the equator. This trend is clearer for spheres with homogeneously distributed radiation sources than it is for central sources. Remarkably, we find three quantities that are invariant with respect to the viewing angle and the rotational velocity: the integrated flux, the escape fraction and the average number of scatterings. These results helped us to construct the outgoing spectra of a rotating sphere as a superposition of spectra coming from a static configuration. This description is useful to describe the main quantitative features of the Monte Carlo simulations. Quantitatively, the main results of our study are summarized as follows.

- In all of our models, rotation induces changes in the line morphology for different values of the angle between the rotation axis and the LoS,  $\theta$ . The changes are such that for a viewing angle perpendicular to the rotation axis, and high rotational velocities the line becomes single peaked.
- The line width increases with rotational velocity. For a viewing angle perpendicular to the rotation axis This change approximately follows the functional form  $\text{FWHM}^2 = \text{FWHM}_0^2 + (V_{\text{max}}/\lambda)^2$ , where  $\text{FWHM}_0$  indicates the line width for the static case and  $\lambda$  is a constant. We have determined this constant to be  $\lambda_c = 0.83 \pm 0.06$  and  $\lambda_h = 0.82 \pm 0.05$  for the central and homogeneous source distributions, respectively.
- At fixed rotational velocity the line width decreases as  $|\mu|$  increases, i.e. the smallest value of the line width is observed for a line of sight parallel to the rotation axis.
- The single peaked line emerges at viewing angles  $\mu \sim 1$  for when the rotational velocity is close to than half the  $\text{FWHM}_0$ .

Comparing our results with recent observed LAEs we find that morphological features such as high central line flux, single peak profiles could be explained by gas bulk rotation present in these LAEs. The definitive and clear impact of rotation on the Ly $\alpha$  morphology suggests that this is an effect that should be taken into account at the moment of interpreting high resolution spectroscopic data. In particular it is relevant to consider the joint effect of rotation the and ubiquitous outflows (M.C. Remolina-Gutierrez et al., in prep.) because rotation can lead to enhanced escape of Ly $\alpha$  at line center, which has also been associated with escape of ionizing (LyC) photons [30, 49]

## Acknowledgments

JNGC acknowledges financial support from Universidad de los Andes. JEFR acknowledges financial support from Vicerrectoria de Investigaciones at Universidad de los Andes through a FAPA grant. We thank the International Summer School on AstroComputing 2012 organized by the University of California High-Performance AstroComputing Center (UC-HiPACC) for providing computational resources where some of the calculations were done. The data, source code and instructions to replicate the results of this paper can be found here <https://github.com/jngaravitoc/RotationLyAlpha>. Most of our code benefits from the work of the IPython and Matplotlib communities [51, 52]. We thank the referee for the suggestions that allowed us to greatly improve and better frame the interpretation of our simulations.

## .1 Analytic Expression for the Ly $\alpha$ Spectrum emerging from Rotating Cloud

Ly $\alpha$  scattering through an optically thick gas cloud that is undergoing solid-body rotation (i.e. in which the angular speed around the rotation axis is identical for each hydrogen atom) proceeds identical as in a static cloud. In order to compute the spectrum emerging from a rotating cloud, we sum the spectra emerging from all surface elements of the cloud, weighted by their intensity. We adopt the geometry shown in Fig A.1 to derive an analytic expression of this emerging spectrum, Note that this geometry differs from the scheme shown in Fig 1 in the main body of the paper. The

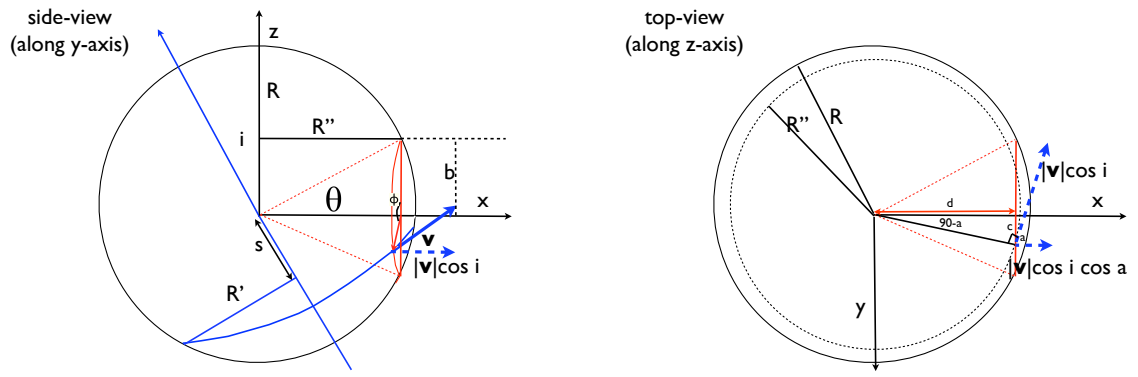


FIGURE 12: Adopted geometry for evaluating the analytic spectrum.

sightline to the observer & rotation axis define the  $x - z$  plane. The *left panel* in Fig A.1 shows the view from the  $y$ -axis. The observer sits along the  $x$  axis. The rotation axis makes an angle  $i$  with respect to the  $z$ -axis. We sum up spectra from individual patches by integrating over the impact parameter  $b$ , and angle  $\phi$ . Each  $(b, \phi)$  corresponds to a point on the sphere. This point has a velocity vector  $\mathbf{v}(b, \phi, i)$ , which we denote with  $\mathbf{v}$  for brevity. The magnitude of  $\mathbf{v}$  is  $|\mathbf{v}| = V_{\max} R'/R$ . Here  $R' = \sqrt{R^2 - s^2}$ , in which  $s$  denotes the distance of the point  $(b, \phi)$  to the plane perpendicular to the rotation axis and through the origin (see the *left panel* of Fig A.1). This distance  $s$  is given by  $s = | -\sin i \sqrt{R^2 - b^2} + b \cos \phi \cos i |$ .

The spectrum of the flux emerging from the surface at point  $(b, \phi)$  is

$$J(x, b, \phi, i) = \frac{\sqrt{\pi}}{\sqrt{24}a\tau_0} \left( \frac{(x - x_b)^2}{1 + \cosh \left[ \sqrt{\frac{2\pi^3}{27}} \frac{|(x - x_b)^3|}{a\tau_0} \right]} \right),$$

where  $x_b \equiv v_b/v_{\text{th}}$ , and  $v_b$  is the component of  $\mathbf{v}$  projected onto the line-of-sight. This component is given by

$$v_b(b, \phi, i) = V_{\text{max}} \frac{\sqrt{R^2 - s^2}}{R} \cos i \cos a, \quad (6)$$

where  $\beta = 90^\circ - a$ . The factor  $\cos i$  accounts for the projection onto the  $x - y$  plane, and the factor  $\cos a$  for the subsequent projection onto the line-of-sight. The *right panel* of Fig. A.1 shows that this angle  $a$  can be computed from

$$\tan \beta = \tan[90^\circ - a] = \frac{c}{d} = \frac{b \sin \phi}{\sqrt{R^2 - b^2}}, \quad (7)$$

In order to compute the total intensity we integrate over  $b$  and  $\phi$  with a weight given by the surface brightness of the sphere at  $(b, \phi)$ ,  $S(b, \phi)$ .

$$J(x, i) = 2\pi \int_0^R db b \int_0^{2\pi} d\phi S(b, \phi) J(x, b, \phi, i) \approx 2\pi \int_0^R db b \int_0^{2\pi} d\phi J(x, b, \phi, i).$$

In the last expression we assume that  $S(b, \phi)$  is constant. This corresponds to  $I(\mu) \propto \mu$  at the surface, where  $\mu$  denotes the cosine of the angle of the propagation direction of the outgoing photon and the normal to the spheres surface: a fixed  $db$  corresponds to a physical length  $ds = db/\mu$  on the sphere. If  $I(\mu)$  were constant, this would imply that the sphere should appear brighter per unit  $b$ . A constant surface brightness profile requires the directional dependence for  $I(\mu) \propto \mu$  to correct for this. Indeed, this is what is expected for the escape of Ly $\alpha$  photons from static, extremely opaque media (see Ahn et al. [44]; their Fig 4 and accompanying discussion). It is worth stressing that this derivation should not be viewed as a complete analytic calculation, and we do not expect perfect agreement: we *assumed* a functional form for the surface brightness profile [or for  $I(\mu)$ ]. Moreover,  $I(\mu)$  itself may depend on frequency  $x$ . In other words, analytic solutions exist for  $J(x) = \int_0^1 I(x, \mu) d\mu$  at the boundary of the sphere, and *approximate* expressions for  $I(\mu) = \int dx I(x, \mu)$ , but *not* for  $I(x, \mu)$  itself. The spectra we obtained from the Monte-Carlo calculations naturally include the proper  $I(x, \mu)$ , and are therefore expected to be more accurate. To further test the assumption of scattering in a rotating medium proceeding as in a static medium we compute the distribution of the outgoing angles  $\mu$ . The results are shown in Figure A.2; it shows that the distribution for  $\mu$  is independent of the rotational velocity and the location over the sphere. The only dependence comes with  $\tau_H$ . For higher values of the optical depth the distribution gets closer to  $I(\mu) \propto \mu$  as expected for a static medium [44].

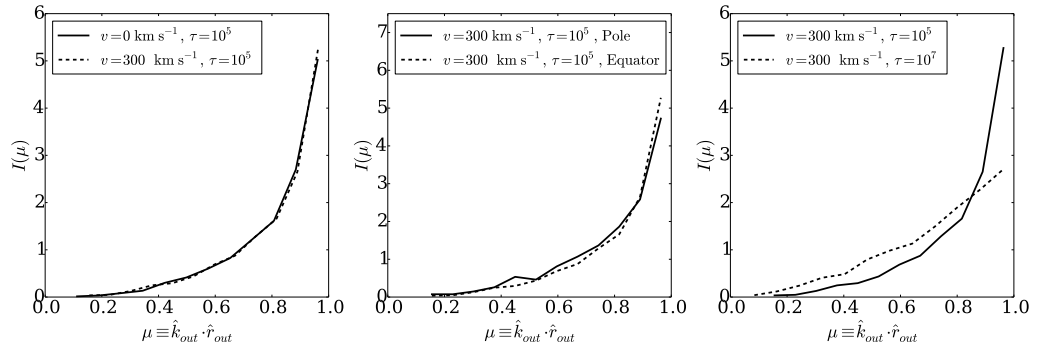


FIGURE 13: Distribution of the cosine of the angle between the propagation direction and a vector normal to the sphere's surface. The distributions have been normalized to unity. Left panel: different rotational velocities; middle panel: different viewing angles; right panel: different optical depths. Only the optical depth has an effect on the distribution of outgoing directions. This is consistent with the assumption that Lyman  $\alpha$  scattering in a medium with solid body rotation proceeds as in a static medium.

## Appendix A

# Analytic Expression for the $\text{Ly}\alpha$ Spectrum emerging from Rotating Cloud

$\text{Ly}\alpha$  scattering through an optically thick gas cloud that is undergoing solid-body rotation (i.e. in which the angular speed around the rotation axis is identical for each hydrogen atom) proceeds identical as in a static cloud. In order to compute the spectrum emerging from a rotating cloud, we sum the spectra emerging from all surface elements of the cloud, weighted by their intensity. We adopt the geometry shown in Fig A.1 to derive an analytic expression of this emerging spectrum, Note that this geometry differs from the scheme shown in Fig 1 in the main body of the thesis. The

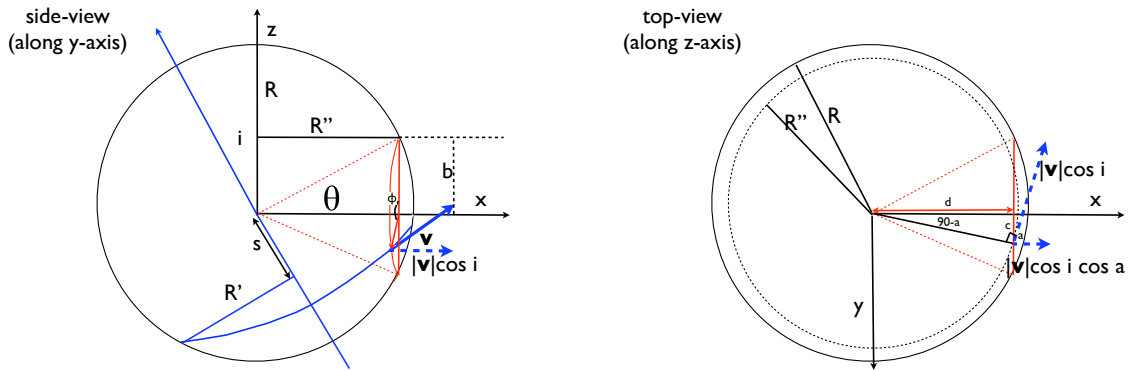


FIGURE A.1: Adopted geometry for evaluating the analytic spectrum.

sightline to the observer & rotation axis define the  $x - z$  plane. The *left panel* in Fig A.1 shows the view from the  $y$ -axis. The observer sits along the  $x$  axis. The rotation axis makes an angle  $i$  with respect to the  $z$ -axis. We sum up spectra from individual patches

by integrating over the impact parameter  $b$ , and angle  $\phi$ . Each  $(b, \phi)$  corresponds to a point on the sphere. This point has a velocity vector  $\mathbf{v}(b, \phi, i)$ , which we denote with  $\mathbf{v}$  for brevity. The magnitude of  $\mathbf{v}$  is  $|\mathbf{v}| = V_{\max} R'/R$ . Here  $R' = \sqrt{R^2 - s^2}$ , in which  $s$  denotes the distance of the point  $(b, \phi)$  to the plane perpendicular to the rotation axis and through the origin (see the *left panel* of Fig A.1). This distance  $s$  is given by  $s = |-\sin i \sqrt{R^2 - b^2} + b \cos \phi \cos i|$ .

The spectrum of the flux emerging from the surface at point  $(b, \phi)$  is

$$J(x, b, \phi, i) = \frac{\sqrt{\pi}}{\sqrt{24}a\tau_0} \left( \frac{(x - x_b)^2}{1 + \cosh \left[ \sqrt{\frac{2\pi^3}{27}} \frac{|(x - x_b)^3|}{a\tau_0} \right]} \right),$$

where  $x_b \equiv v_b/v_{\text{th}}$ , and  $v_b$  is the component of  $\mathbf{v}$  projected onto the line-of-sight. This component is given by

$$v_b(b, \phi, i) = V_{\max} \frac{\sqrt{R^2 - s^2}}{R} \cos i \cos a, \quad (\text{A.1})$$

where  $\beta = 90^\circ - a$ . The factor  $\cos i$  accounts for the projection onto the  $x - y$  plane, and the factor  $\cos a$  for the subsequent projection onto the line-of-sight. The *right panel* of Fig. A.1 shows that this angle  $a$  can be computed from

$$\tan \beta = \tan[90^\circ - a] = \frac{c}{d} = \frac{b \sin \phi}{\sqrt{R^2 - b^2}}, \quad (\text{A.2})$$

In order to compute the total intensity we integrate over  $b$  and  $\phi$  with a weight given by the surface brightness of the sphere at  $(b, \phi)$ ,  $S(b, \phi)$ .

$$J(x, i) = 2\pi \int_0^R db \, b \int_0^{2\pi} d\phi \, S(b, \phi) J(x, b, \phi, i) \approx 2\pi \int_0^R db \, b \int_0^{2\pi} d\phi \, J(x, b, \phi, i).$$

In the last expression we assume that  $S(b, \phi)$  is constant. This corresponds to  $I(\mu) \propto \mu$  at the surface, where  $\mu$  denotes the cosine of the angle of the propagation direction of the outgoing photon and the normal to the sphere's surface: a fixed  $db$  corresponds to a physical length  $ds = db/\mu$  on the sphere. If  $I(\mu)$  were constant, this would imply that the sphere should appear brighter per unit  $b$ . A constant surface brightness profile requires the directional dependence for  $I(\mu) \propto \mu$  to correct for this. Indeed, this is what is expected for the escape of Ly $\alpha$  photons from static, extremely opaque media (see Ahn et al. [44]; their Fig 4 and accompanying discussion). It is worth stressing that this derivation should not be viewed as a complete analytic calculation, and we do not expect perfect agreement: we *assumed* a functional form for the surface brightness profile [or for  $I(\mu)$ ]. Moreover,  $I(\mu)$  itself may depend on frequency  $x$ . In other words, analytic solutions exist for  $J(x) = \int_0^1 I(x, \mu) d\mu$  at the boundary of the sphere, and *approximate* expressions for  $I(\mu) = \int dx I(x, \mu)$ , but *not* for  $I(x, \mu)$  itself. The spectra we obtained



from the Monte-Carlo calculations naturally include the proper  $I(x, \mu)$ , and are therefore expected to be more accurate. To further test the assumption of scattering in a rotating medium proceeding as in a static medium we compute the distribution of the outgoing angles  $\mu$ . The results are shown in Figure A.2; it shows that the distribution for  $\mu$  is independent of the rotational velocity and the location over the sphere. The only dependence comes with  $\tau_H$ . For higher values of the optical depth the distribution gets closer to  $I(\mu) \propto \mu$  as expected for a static medium [44].

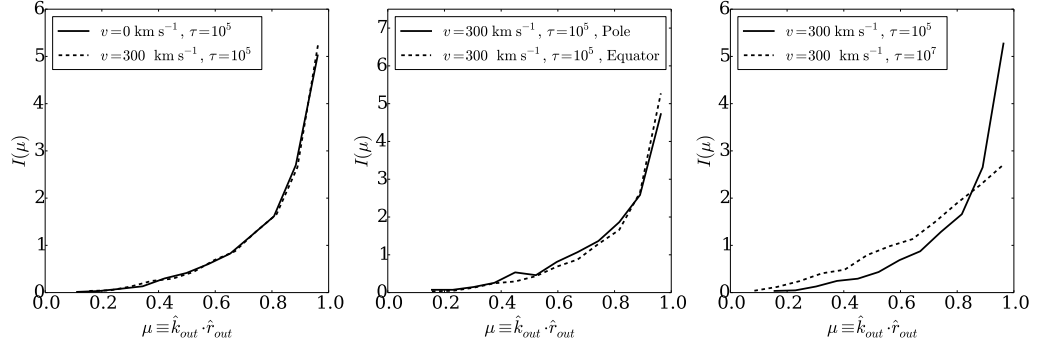


FIGURE A.2: Distribution of the cosine of the angle between the propagation direction and a vector normal to the sphere's surface. The distributions have been normalized to unity. Left panel: different rotational velocities; middle panel: different viewing angles; right panel: different optical depths. Only the optical depth has an effect on the distribution of outgoing directions. This is consistent with the assumption that Lyman  $\alpha$  scattering in a medium with solid body rotation proceeds as in a static medium.

# Bibliography

- [1] R. B. Partridge and P. J. E. Peebles. Are Young Galaxies Visible? , 147:868, March 1967. doi: 10.1086/149079.
- [2] D. E. Osterbrock. The Escape of Resonance-Line Radiation from an Optically Thick Nebula. , 135:195, January 1962. doi: 10.1086/147258.
- [3] T. F. Adams. The Escape of Resonance-Line Radiation from Extremely Opaque Media. , 174:439, June 1972. doi: 10.1086/151503.
- [4] J. P. Harrington. The scattering of resonance-line radiation in the limit of large optical depth. , 162:43, 1973.
- [5] D. A. Neufeld. The transfer of resonance-line radiation in static astrophysical media. , 350:216–241, February 1990. doi: 10.1086/168375.
- [6] S. Djorgovski and D. J. Thompson. Searches for Primeval Galaxies. In B. Barbuy and A. Renzini, editors, *The Stellar Populations of Galaxies*, volume 149 of *IAU Symposium*, page 337, 1992.
- [7] M. D. Lehnert, N. P. H. Nesvadba, J.-G. Cuby, A. M. Swinbank, S. Morris, B. Clément, C. J. Evans, M. N. Bremer, and S. Basa. Spectroscopic confirmation of a galaxy at redshift  $z = 8.6$ . , 467:940–942, October 2010. doi: 10.1038/nature09462.
- [8] G. B. Brammer, P. G. van Dokkum, G. D. Illingworth, R. J. Bouwens, I. Labbé, M. Franx, I. Momcheva, and P. A. Oesch. A Tentative Detection of an Emission Line at  $1.6 \mu\text{m}$  for the  $z \sim 12$  Candidate UDFj-39546284. , 765:L2, March 2013. doi: 10.1088/2041-8205/765/1/L2.
- [9] M. Dijkstra and R. Kramer. Line transfer through clumpy, large-scale outflows: Ly  $\alpha$  absorption and haloes around star-forming galaxies. , 424:1672–1693, August 2012. doi: 10.1111/j.1365-2966.2012.21131.x.
- [10] P. Laursen, J. Sommer-Larsen, and A. C. Andersen. Ly $\alpha$  Radiative Transfer with Dust: Escape Fractions from Simulated High-Redshift Galaxies. , 704:1640–1656, October 2009. doi: 10.1088/0004-637X/704/2/1640.

- [11] A. Verhamme, D. Schaerer, and A. Maselli. 3D Ly $\alpha$  radiation transfer. I. Understanding Ly $\alpha$  line profile morphologies. , 460:397–413, December 2006. doi: 10.1051/0004-6361:20065554.
- [12] J. E. Forero-Romero, G. Yepes, S. Gottlöber, S. R. Knollmann, A. J. Cuesta, and F. Prada. CLARA’s view on the escape fraction of Lyman  $\alpha$  photons in high-redshift galaxies. , 415:3666–3680, August 2011. doi: 10.1111/j.1365-2966.2011.18983.x.
- [13] J. M. Mas-Hesse, D. Kunth, G. Tenorio-Tagle, C. Leitherer, R. J. Terlevich, and E. Terlevich. Ly $\alpha$  Emission in Starbursts: Implications for Galaxies at High Redshift. , 598:858–877, December 2003. doi: 10.1086/379116.
- [14] G. Östlin, M. Hayes, F. Duval, A. Sandberg, T. Rivera-Thorsen, T. Marquart, I. Orlitová, A. Adamo, J. Melinder, L. Guaita, H. Atek, J. M. Cannon, P. Gruyters, E. C. Herenz, D. Kunth, P. Laursen, J. M. Mas-Hesse, G. Micheva, H. Otí-Flóranes, S. A. Pardy, M. M. Roth, D. Schaerer, and A. Verhamme. The Ly $\alpha$  Reference Sample. I. Survey Outline and First Results for Markarian 259. , 797:11, December 2014. doi: 10.1088/0004-637X/797/1/11.
- [15] P. Laursen. Lyman  $\{\alpha\}$  radiative transfer in the high-redshift, dusty Universe. *ArXiv e-prints*, December 2010.
- [16] M. Dijkstra. Lyman Alpha Emitting Galaxies as a Probe of Reionization. *ArXiv e-prints*, *arXiv:1406.7292*, June 2014.
- [17] R. Kotak, W. P. S. Meikle, D. Farrah, C. L. Gerardy, R. J. Foley, S. D. Van Dyk, C. Fransson, P. Lundqvist, J. Sollerman, R. Fesen, A. V. Filippenko, S. Mattila, J. M. Silverman, A. C. Andersen, P. A. Höflich, M. Pozzo, and J. C. Wheeler. Dust and The Type II-Plateau Supernova 2004et. , 704:306–323, October 2009. doi: 10.1088/0004-637X/704/1/306.
- [18] K. E. K. Coppin, I. Smail, D. M. Alexander, A. Weiss, F. Walter, A. M. Swinbank, T. R. Greve, A. Kovacs, C. De Breuck, M. Dickinson, E. Ibar, R. J. Ivison, N. Reddy, H. Spinrad, D. Stern, W. N. Brandt, S. C. Chapman, H. Dannerbauer, P. van Dokkum, J. S. Dunlop, D. Frayer, E. Gawiser, J. E. Geach, M. Huynh, K. K. Knudsen, A. M. Koekemoer, B. D. Lehmer, K. M. Menten, C. Papovich, H.-W. Rix, E. Schinnerer, J. L. Wardlow, and P. P. van der Werf. A submillimetre galaxy at  $z = 4.76$  in the LABOCA survey of the Extended Chandra Deep Field-South. , 395:1905–1914, June 2009. doi: 10.1111/j.1365-2966.2009.14700.x.
- [19] P. Laursen, F. Duval, and G. Östlin. On the (Non-)Enhancement of the Ly $\alpha$  Equivalent Width by a Multiphase Interstellar Medium. , 766:124, April 2013. doi: 10.1088/0004-637X/766/2/124.

- [20] M. A. Schenker, D. P. Stark, R. S. Ellis, B. E. Robertson, J. S. Dunlop, R. J. McLure, J.-P. Kneib, and J. Richard. Keck Spectroscopy of Faint  $3 < z < 8$  Lyman Break Galaxies: Evidence for a Declining Fraction of Emission Line Sources in the Redshift Range  $6 < z < 8$ . , 744:179, January 2012. doi: 10.1088/0004-637X/744/2/179.
- [21] D. Sobral, J. Matthee, B. Darvish, D. Schaerer, B. Mobasher, H. Röttgering, S. Santos, and S. Hemmati. Evidence for PopIII-like stellar populations in the most luminous Lyman- $\alpha$  emitters at the epoch of re-ionisation: spectroscopic confirmation. *ArXiv e-prints*, April 2015.
- [22] G. B. Rybicki and A. P. Lightman. *Radiative processes in astrophysics*. 1979.
- [23] W. Unno. Theoretical Line Contour of the Lyman Alpha Radiation of Ionized Helium and the Excitation of Bowen Lines in Planetary Nebulae. , 7:81, 1955.
- [24] M. Dijkstra, Z. Haiman, and M. Spaans. Ly $\alpha$  Radiation from Collapsing Protogalaxies. I. Characteristics of the Emergent Spectrum. , 649:14–36, September 2006. doi: 10.1086/506243.
- [25] A. Verhamme, Y. Dubois, J. Blaizot, T. Garel, R. Bacon, J. Devriendt, B. Guiderdoni, and A. Slyz. Lyman- $\alpha$  emission properties of simulated galaxies: interstellar medium structure and inclination effects. , 546:A111, October 2012. doi: 10.1051/0004-6361/201218783.
- [26] H. Yajima, Y. Li, Q. Zhu, T. Abel, C. Gronwall, and R. Ciardullo. Were Progenitors of Local L\* Galaxies Ly $\alpha$  Emitters at High Redshift? , 754:118, August 2012. doi: 10.1088/0004-637X/754/2/118.
- [27] S.-H. Ahn, H.-W. Lee, and H. M. Lee. P Cygni type Ly $\alpha$  from starburst galaxies. , 340:863–869, April 2003. doi: 10.1046/j.1365-8711.2003.06353.x.
- [28] M. Hansen and S. P. Oh. Lyman  $\alpha$  radiative transfer in a multiphase medium. , 367:979–1002, April 2006. doi: 10.1111/j.1365-2966.2005.09870.x.
- [29] Z. Zheng and J. Wallace. Anisotropic Lyman-alpha Emission. *ArXiv e-prints*, August 2013.
- [30] C. Behrens, M. Dijkstra, and J. C. Niemeyer. Beamed Ly $\alpha$  emission through outflow-driven cavities. , 563:A77, March 2014. doi: 10.1051/0004-6361/201322949.
- [31] J. E. Forero-Romero, G. Yepes, S. Gottlöber, and F. Prada. Modelling the fraction of Lyman break galaxies with strong Lyman  $\alpha$  emission at  $5 \leq z \leq 7$ . , 419:952–958, January 2012. doi: 10.1111/j.1365-2966.2011.19744.x.

- [32] L. A. Barnes, M. G. Haehnelt, E. Tescari, and M. Viel. Galactic winds and extended Ly $\alpha$  emission from the host galaxies of high column density quasi-stellar object absorption systems. , 416:1723–1738, September 2011. doi: 10.1111/j.1365-2966.2011.18789.x.
- [33] J. E. Rhoads, S. Malhotra, A. Dey, D. Stern, H. Spinrad, and B. T. Jannuzi. First Results from the Large-Area Lyman Alpha Survey. , 545:L85–L88, December 2000. doi: 10.1086/317874.
- [34] E. Gawiser, H. Francke, K. Lai, K. Schawinski, C. Gronwall, R. Ciardullo, R. Quadri, A. Orsi, L. F. Barrientos, G. A. Blanc, G. Fazio, and J. J. Feldmeier. Ly $\alpha$ -Emitting Galaxies at  $z = 3.1$ : L\* Progenitors Experiencing Rapid Star Formation. *ApJ*, *archivePrefix* = "arXiv", *eprint* = 0710.2697, *keywords* = Galaxies: Evolution, Galaxies: Formation, Galaxies: High-Redshift, Cosmology: Large-Scale Structure of Universe, *year* = 2007, *month* = dec, *volume* = 671, *pages* = 278-284, *doi* = 10.1086/522955, *adsurl* = <http://adsabs.harvard.edu/abs/2007ApJ...671..278G>, *adsnote* = Provided by the SAO/NASA Astrophysics Data System.
- [35] R. S. Koehler, P. Schuecker, and K. Gebhardt. Probing dark energy with baryonic acoustic oscillations at high redshifts. *AAP*, 462:7–20, January 2007. doi: 10.1051/0004-6361:20065649.
- [36] M. Ouchi, K. Shimasaku, M. Akiyama, C. Simpson, T. Saito, Y. Ueda, H. Furusawa, K. Sekiguchi, T. Yamada, T. Kodama, N. Kashikawa, S. Okamura, M. Iye, T. Takata, M. Yoshida, and M. Yoshida. The Subaru/XMM-Newton Deep Survey (SXDS). IV. Evolution of Ly $\alpha$  Emitters from  $z=3.1$  to 5.7 in the 1 deg<sup>2</sup> Field: Luminosity Functions and AGN. , 176:301–330, June 2008. doi: 10.1086/527673.
- [37] T. Yamada, Y. Nakamura, Y. Matsuda, T. Hayashino, R. Yamauchi, N. Morimoto, K. Kousai, and M. Umemura. Panoramic Survey of Ly $\alpha$  Emitters at  $z = 3.1$ . , 143: 79, April 2012. doi: 10.1088/0004-6256/143/4/79.
- [38] M. A. Schenker, D. P. Stark, R. S. Ellis, B. E. Robertson, J. S. Dunlop, R. J. McLure, J.-P. Kneib, and J. Richard. Keck Spectroscopy of Faint  $3 < z < 8$  Lyman Break Galaxies: Evidence for a Declining Fraction of Emission Line Sources in the Redshift Range  $6 < z < 8$ . *ApJ*, 744:179, January 2012. doi: 10.1088/0004-637X/744/2/179.
- [39] S. L. Finkelstein, C. Papovich, M. Dickinson, M. Song, V. Tilvi, a. M. Koekoer, K. D. Finkelstein, B. Mobasher, H. C. Ferguson, M. Giavalisco, N. Reddy, M. L. N. Ashby, a. Dekel, G. G. Fazio, a. Fontana, N. a. Grogin, J.-S. Huang,

- D. Kocevski, M. Rafelski, B. J. Weiner, and S. P. Willner. A galaxy rapidly forming stars 700 million years after the Big Bang at redshift 7.51. *Nature*, 502 (7472):524–527, October 2013. ISSN 0028-0836. doi: 10.1038/nature12657. URL <http://www.nature.com/doifinder/10.1038/nature12657>.
- [40] A. Loeb and G. B. Rybicki. Scattered Ly $\alpha$  Radiation around Sources before Cosmological Reionization. , 524:527–535, October 1999. doi: 10.1086/307844.
- [41] L. H. Auer. Transfer of Lyman Alpha in Diffuse Nebulae. , 153:783, September 1968. doi: 10.1086/149705.
- [42] L. W. Avery and L. L. House. An Investigation of Resonance-Line Scattering by the Monte Carlo Technique. , 152:493, May 1968. doi: 10.1086/149566.
- [43] S.-H. Ahn, H.-W. Lee, and H. M. Lee. Ly Alpha Transfer in a Thick, Dusty, and Static Medium. *Journal of Korean Astronomical Society*, 33:29–36, April 2000.
- [44] S.-H. Ahn, H.-W. Lee, and H. M. Lee. Ly $\alpha$  Line Formation in Starbursting Galaxies. I. Moderately Thick, Dustless, and Static H I Media. , 554:604–614, June 2001. doi: 10.1086/321374.
- [45] Z. Zheng and J. Miralda-Escudé. Monte Carlo Simulation of Ly $\alpha$  Scattering and Application to Damped Ly $\alpha$  Systems. , 578:33–42, October 2002. doi: 10.1086/342400.
- [46] A. Orsi, C. G. Lacey, and C. M. Baugh. Can galactic outflows explain the properties of Ly  $\alpha$  emitters? , 425:87–115, September 2012. doi: 10.1111/j.1365-2966.2012.21396.x.
- [47] T. Garel, J. Blaizot, B. Guiderdoni, D. Schaerer, A. Verhamme, and M. Hayes. Modelling high redshift Lyman  $\alpha$  emitters. , 422:310–325, May 2012. doi: 10.1111/j.1365-2966.2012.20607.x.
- [48] C. Behrens and J. Niemeyer. Effects of Lyman-alpha scattering in the IGM on clustering statistics of Lyman-alpha emitters. , 556:A5, August 2013. doi: 10.1051/0004-6361/201321172.
- [49] A. Verhamme, I. Orlitova, D. Schaerer, and M. Hayes. On the use of Lyman-alpha to detect Lyman continuum leaking galaxies. *ArXiv e-prints*, April 2014.
- [50] P. Dayal and A. Ferrara. Ly $\alpha$  emitters and Lyman-break galaxies: dichotomous twins. , 421:2568–2579, April 2012. doi: 10.1111/j.1365-2966.2012.20486.x.
- [51] Fernando Pérez and Brian E. Granger. Ipython: a system for interactive scientific computing. *Computing in Science and Engineering*, 9(3):21–29, May 2007. ISSN 1521-9615. doi: 10.1109/MCSE.2007.53. URL <http://ipython.org>.

- 
- [52] J. D. Hunter. Matplotlib: A 2d graphics environment. *Computing In Science & Engineering*, 9(3):90–95, 2007.